

1 **Highly resolved mapping of NO₂ vertical column densities from** 2 **GeoTASO measurements over a megacity and industrial area during** 3 **the KORUS-AQ campaign**

4 Gyo-Hwang Choo¹, Kyunghwa Lee¹, Hyunkee Hong^{1*}, Ukkyo Jeong^{2,3}, Wonei Choi⁴, Scott J. Janz³

5 ¹Environmental Satellite Center, National Institute of Environmental Research, Hwangyeong-ro 42, Seo-gu, Incheon, Republic
6 of Korea, 22689

7 ²Earth System Science Interdisciplinary Center, University of Maryland, College Park, Maryland, USA 20740

8 ³NASA Goddard Space Flight Center, Greenbelt, Maryland, USA, 20771

9 ⁴Division of Earth Environmental System Science, Major of Spatial Information Engineering, Pukyong National University,
10 Busan 48513, South Korea

11 *Correspondence to:* Hyunkee Hong; Tel: +82 32 560 8437; Fax: +82 32 560 8460; E-mail address: wanju77@korea.kr

12 **Abstract.** The Korea-United States Air Quality (KORUS-AQ) campaign is a joint study between the United States National
13 Aeronautics and Space Administration (NASA) and the South Korea National Institute of Environmental Research (NIER) to
14 monitor megacity and transboundary air pollution around the Korean Peninsula using airborne and ground-based
15 measurements. Here, tropospheric nitrogen dioxide (NO₂) slant column density (SCD) measurements were retrieved from
16 Geostationary Trace and Aerosol Sensor Optimization (GeoTASO) L1B data during the KORUS-AQ campaign (May 1 to
17 June 10, 2016). The retrieved SCDs were converted to tropospheric vertical column densities using the air mass factor (AMF)
18 obtained from a radiative transfer calculation with trace gas profiles and aerosol property inputs simulated with the Community
19 Multiscale Air Quality (CMAQ) model and surface reflectance data obtained from the Moderate Resolution Imaging
20 Spectroradiometer (MODIS). For the first time, we examine highly resolved (250 m × 250 m resolution) tropospheric NO₂
21 over the Seoul and Busan metropolitan regions, and the industrial regions of Anmyeon. We reveal that the maximum NO₂
22 VCDs were 4.94×10^{16} and 1.46×10^{17} molecules cm⁻² at 9 AM and 3 PM over Seoul, respectively, 6.86×10^{16} and $4.89 \times$
23 10^{16} molecules cm⁻² in the morning and afternoon over Busan, respectively, and 1.64×10^{16} molecules cm⁻² over Anmyeon.
24 The VCDs retrieved from the GeoTASO airborne instrument were well correlated with those obtained from the Ozone
25 Monitoring Instrument (OMI) ($r = 0.70$), NASA's Pandora Spectrometer System ($r = 0.79$), and NO₂ mixing ratios obtained
26 from in situ measurements ($r = 0.45$ in the morning, $r = 0.81$ in the afternoon over the Seoul, and $r > 0.78$ over Busan). Based
27 on our results, GeoTASO is useful for identifying hotspots of NO₂ and its spatial distribution in highly populated cities and
28 industrial areas.

29 1 Introduction

30 Nitrogen dioxide (NO₂) is one of the most important atmospheric trace gases and plays a key role in aerosol production and
31 tropospheric ozone photochemistry (Boersma et al., 2004; Richter et al., 2005). Furthermore, high NO₂ concentrations in the
32 atmosphere have adverse effects on human health, such as respiratory infections, domestic heating, and associated symptoms
33 (Brauer et al., 2002; Latza et al., 2009).

34 The major sources of NO₂ in the atmosphere are from fossil fuel combustion from vehicles and thermal power plants, lightning,
35 flash production, and biogenic soil processes. In addition, it has been found that NO₂ concentrations are highly correlated with
36 population size (Lamsal et al., 2013). The implementation of emission control technology and environmental regulation has
37 led to a decrease in surface NO₂ concentrations in Western Europe, the United States, and Japan in the last few decades (Richter
38 et al., 2005). The NO₂ concentration over major metropolitan cities in South Korea and China are over 3 times larger than over
39 similarly sized cities in Europe and United States, despite NO₂ concentration decreasing in China and South Korea (de Foy et
40 al., 2016, Choo et al., 2020).

41 To date, several low-orbit space borne sensors, such as the Global Ozone Monitoring Experiment (GOME) (Burrows et al.,
42 1999), the Scanning Imaging Spectrometer for Atmospheric Cartography (SCIAMACHY) (Burrows et al., 1995), the Ozone
43 Monitoring Instrument (OMI) (Levelt et al., 2006), the GOME-2 (Callies et al., 2000), and the Tropospheric Monitoring
44 Instrument (TROPOMI) (Veefkind et al., 2012), have monitored atmospheric ozone and its precursors including NO₂ and
45 formaldehyde (HCHO) as a proxy for volatile organic compounds (VOCs). Furthermore, the Geostationary Environment
46 Monitoring Spectrometer (GEMS) (Choi et al., 2018; Kim et al., 2020), which was launched on February 18, 2020, will form
47 a constellation of geostationary satellites including the upcoming Tropospheric Emission: Monitoring of Pollution (TEMPO)
48 (Zoogman et al., 2017) and Sentinel-4 platforms, to continuously observe the air quality of the Northern Hemisphere during
49 the daytime.

50 NO₂ retrievals from space borne hyperspectral measurements are typically conducted using the differential optical absorption
51 spectroscopy (DOAS) method (Platt and Stutz, 2008) to first retrieve the view-dependent slant column density (SCD), and
52 then radiative transfer models are used to determine the vertical column density (VCD) using an air mass factor (AMF)
53 correction. Previous and ongoing space borne instruments use various radiative transfer codes and model input assumptions to
54 calculate NO₂ AMF values at fairly coarse spatial resolution. Because the AMF weighting has a large impact on NO₂ retrievals
55 using the DOAS method, it is important to use model input assumptions that most accurately match the viewing and
56 atmospheric conditions. Several studies have demonstrated the sensitivity of AMF calculations to inaccurate model input
57 parameters (e.g., *a priori* NO₂ vertical profile and aerosol properties) and *a priori* data (cloud information and surface
58 reflectance) (Leitão et al., 2010; Hong et al., 2017; Lorente et al., 2017; Boersma et al., 2018). NO₂ retrievals have also been
59 consistently conducted based on surface remote sensing measurements including the Multi-Axis DOAS (MAX-DOAS),
60 Système D'Analyse par Observations Zénithales (SAOZ) spectrometer (Pastel et al., 2014), and Pandora (Herman et al., 2009)

61 systems. These ground-based measurements can be used as validation references for both airborne and space borne
62 measurements.

63 Furthermore, NO₂ retrievals from airborne remote sensing instruments, such as the Geostationary Coast and Air Pollution
64 Event (GEO-CAPE) Airborne Simulator (GCAS) (Kowalewski and Janz, 2014), the Heidelberg Airborne Imaging DOAS
65 Instrument (HAIDI) (General et al., 2014), the Geostationary Trace gas and Aerosol Sensor Optimization (GeoTASO) (Leitch
66 et al., 2014), the Airborne Prism Experiment (APEX; Popp et al., 2012), the Airborne Imaging DOAS instrument for
67 Measurements of Atmospheric Pollution (AirMAP; Meier et al., 2017; Schönhardt et al., 2015), the Small Whiskbroom Imager
68 for atmospheric composition monitorinG (SWING; Merlaud et al. 2018), and the Spectrolite Breadboard Instrument (SBI;
69 Vlemmix et al., 2017; Tack et al., 2019) have also been performed to identify local emission sources and obtain highly resolved
70 horizontal NO₂ distributions.

71 Observations using airborne measurements have an advantage as they enable the observation of horizontal distributions of
72 trace gases at resolutions higher than space-based satellites and provide data over a wider area than ground-based observations.
73 For example, Nowlan et al. (2018) retrieved tropospheric NO₂ VCDs over Houston, Texas, during the Deriving Information
74 on Surface Conditions from Column and Vertically Resolved Observations Relevant to Air Quality (DISCOVER-AQ)
75 campaign and identified a high correlation with data retrieved from Pandora. Popp et al. (2012) also presented the morning
76 and afternoon NO₂ spatial distribution in Zurich, Switzerland, using APEX. Tack et al. (2017) have conducted high-resolution
77 mapping of NO₂ over three Belgium cities (Antwerp, Brussels, and Liège) using APEX. Judd et al. (2020) and Tack et al.
78 (2021) compared NO₂ VCDs retrieved from GCAS/GeoTASO and APEX with those obtained from TROPOMI over New
79 York City and Antwerp and Brussels, respectively. Merlaud et al. (2013) observed NO₂ VCDs in Turceni over Romania using
80 SWING mounted on an unmanned aerial vehicle (UAV) during the Airborne Romanian Measurements of Aerosols and Trace
81 gases (AROMAT) campaign. These existing NO₂ retrievals, using airborne measurements, have been useful for constraining
82 regional air quality models due to the highly resolved source identification and the ability to tie these results to the ground-
83 based observations.

84 This work focuses on airborne NO₂ retrievals from GeoTASO. This instrument was developed by Ball Aerospace to reduce
85 mission risk for the UV-VIS air quality measurements from geostationary orbit for the GEMS and TEMPO missions (Leitch
86 et al., 2014). The retrieval of NO₂, SO₂, and HCHO observed from GeoTASO L1B data using DOAS and principal component
87 analysis (PCA) (Wold et al., 1987) was conducted through the DISCOVER-AQ and KOREa-United States Air Quality
88 (KORUS-AQ) campaigns (Nowlan et al., 2016; Judd et al., 2018; Choi et al., 2020; Chong et al., 2020). The KORUS-AQ
89 campaign is a joint study between the National Institute of Environmental Research (NIER) and National Aeronautics and
90 Space Administration (NASA) to monitor megacity air pollution and transboundary pollution, and to prepare for geostationary
91 satellite (i.e., GEMS, TEMPO, and Sentinel-4) air quality observability (of trace gases and aerosols), organized from May to
92 June 2016.

93 Although surface NO₂ concentrations in South Korea are high due to high population density, high traffic volumes, and many
94 industrial complexes and thermal power plants, and whereas NO₂ retrieval studies using airborne and ground measurements

over North America, Europe, China, and Japan have been conducted, data for South Korea remain limited. The specific aims of this study are as follows:

- (1) To retrieve tropospheric NO₂ vertical column data using GeoTASO measurements over polluted regions of the Seoul and Busan metropolitan areas and the Anmyeon industrial regions of the Korean Peninsula.
- (2) To estimate NO₂ VCD uncertainties using error propagation accounting for spectral fitting errors and AMF uncertainties associated with input data errors, including aerosol optical depth (AOD), single scattering albedo (SSA), aerosol loading height (ALH), and surface reflectance.
- (3) To compare NO₂ VCDs retrieved from GeoTASO and those obtained from OMI and ground-based Pandora instruments, as well as surface in situ measurements.

2 KORUS-AQ campaign area, measurements, and model simulation

2.1 Campaign area

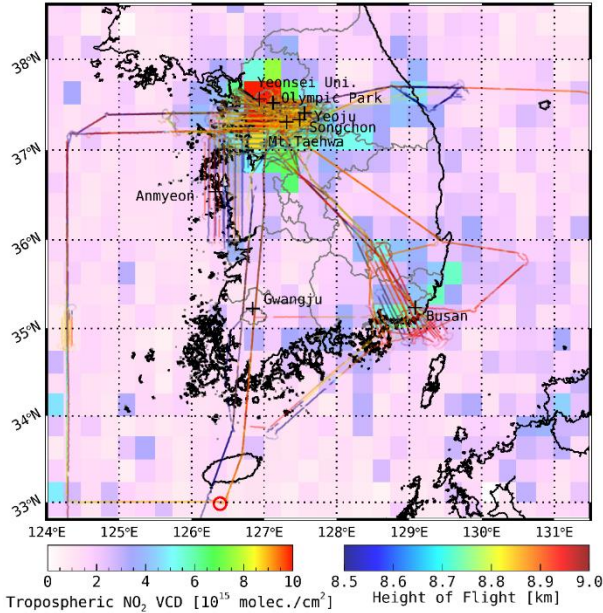


Figure 1. Flight paths of the NASA LaRC B200 aircraft carrying GeoTASO and the average tropospheric NO₂ VCDs obtained from OMI gridded to a 0.25°×0.25° horizontal grid during the KORUS-AQ campaign period. The line colour represents flight height. In this period, the GeoTASO observations focused on megacities (Seoul and Busan) and industrial complex area (Anmyeon) with high tropospheric NO₂ concentrations. The reference spectrum for spectral fitting is obtained from the radiation data under the Jeju Island (marked with red circle).

The Korean Peninsula, located on the Asia-Pacific coast, has a complex atmospheric environment by local emissions and long-range transport under appropriate weather conditions (Jeong et al., 2017; NIER and NASA, 2020; Choo et al., 2021). In

115 particular, Seoul, the capital of South Korea, and the metropolitan area are densely populated, and power plants and industrial
 116 activities on the northwest coast are carried out, which emits relatively large amounts of pollutants. The KORUS-AQ campaign
 117 conducted three-dimensional observations, including ground-based remote, aircraft, satellite observation, and air quality
 118 modelling, to understand the complex air quality and interpret the observations of GEMS launched in 2020. The KORUS-AQ
 119 campaign period was from May 2 to June 10, 2016. During the KORUS-AQ campaign, measurements of air pollutants were
 120 carried out by using the GeoTASO on board the NASA Langley Research Center B200 aircraft to monitor air quality and long-
 121 range transport of pollutants over the Korean Peninsula (NIER and NASA, 2020). The GeoTASO observations conducted a
 122 total of 30 times over 23 days out of 40 days. Most observations were made once or twice a day. Each flight were planned and
 123 conducted on a day when weather conditions were fine and flight hours were approximately 2–4 hours. **Flight information on**
 124 **the date of aircraft observation can be found in detail at [http://www-air.larc.nasa.gov/missions/korus-aq/docs/KORUS-](http://www-air.larc.nasa.gov/missions/korus-aq/docs/KORUS-AQ_Flight_Summaries_ID122.pdf)**
 125 **[AQ_Flight_Summaries_ID122.pdf](http://www-air.larc.nasa.gov/missions/korus-aq/docs/KORUS-AQ_Flight_Summaries_ID122.pdf).** Figure 1 shows the flight routes of B200 and the tropospheric NO₂ VCDs obtained from
 126 the OMI during the campaign period. The observations were concentrated in the metropolitan areas of Seoul and Busan and
 127 the industrial areas of Anmyeon, with a flight altitude of 8,000–9,000 m.
 128 As shown in Fig. 1, GeoTASO observations were conducted focusing on highly NO₂-polluted regions in the Seoul and Busan
 129 metropolitan areas and the **Anmyeon region** during the KORUS-AQ campaign. The Seoul metropolitan area (Seoul Special
 130 City, Gyeonggi Province, and Incheon City) is one of the most densely populated areas worldwide, with a population of
 131 approximately 20 million in 2016. Busan is the second-largest city in South Korea, with a population of approximately 3.4
 132 million in 2016. Anmyeon is located southwest of Seoul with petrochemical complexes, steel mill works, and thermal power
 133 stations in this area. The background colour in Fig. 1 represents the average NO₂ VCD obtained from the OMI during the
 134 KORUS-AQ campaign period, showing over 1×10^{16} molecules cm⁻² over the Seoul metropolitan area. **The OMI data obtained**
 135 **by the Level 2.0 OMNO2 version 3.0 and downloaded from the NASA's Earthdata search**
 136 **(<http://search.earthdata.nasa.gov/search/>).** We calculated the arithmetic means of the tropospheric NO₂ VCDs, similar to Choo
 137 et al. (2020), to obtain the grid data (0.25° × 0.25°) during KORUS-AQ period. The average tropospheric NO₂ VCD data were
 138 excluded from 30 May 2016 to 9 Jun 2016, when the OMI data did not exist during the campaign period.

139 **2.2 Pandora**

140 NO₂ VCDs retrieved from the GeoTASO were validated using those from NASA's Pandora Spectrometer system. The Pandora
 141 spectrometer is a hyper-spectrometer that can provide direct sun measurements of UV/Vis spectra (280–525 nm with a full
 142 width at half maximum (FWHM) of 0.6 nm) for observing atmospheric trace gases. During the KORUS-AQ, eight Pandora
 143 instruments monitored NO₂ and **ozone (O₃)** VCD as depicted by plus symbols in Fig. 1. The retrieved data are available on the
 144 KORUS-AQ pages of NASA's Goddard Space Flight Center website
 145 (<https://avdc.gsfc.nasa.gov/pub/DSCOVER/Pandora/DATA/KORUS-AQ/>). We compared NO₂ VCDs obtained from five
 146 Pandora measurement (Busan university: 35.24 °N, 129.08 °E; Olympic park: 37.52 °N, 127.13 °E; Songchon: 37.41 °N,

127.56 °E; Yeosu: 37.34 °N, 127.49 °E; Yonsei University: 37.56 °N, 126.93 °E) within 0.05 degree and 30 min with those from GeoTASO. Because NO₂ has a short atmospheric lifetime, especially during the summer (Shah et al., 2020), its spatial and temporal distributions vary notably. A detailed description of Pandora’s operation during the KORUS-AQ campaign has been previously reported (Herman et al., 2018; Spinei et al., 2018).

2.3 Ground-based in situ NO₂ measurement

Although the basic physical quantity of VCD and surface mixing ratio from in-situ measurements are different, comparison of their spatiotemporal variations provides useful information for deriving surface air quality from airborne instruments (e.g., Jeong and Hong, 2021a; 2021b and references therein). In this study, we compare the NO₂ VCDs (molecules cm⁻²) retrieved from GeoTASO to surface mixing ratios measured by ground-based in-situ monitoring network over South Korea (i.e., Air-Korea, a national real-time air quality network; <https://www.airkorea.or.kr/>). The instruments utilize the chemiluminescence method (Kley and McFarland, 1980), and approximately 400 air quality monitoring sites in Korea are registered in the system, providing hourly surface NO₂ concentrations. We compared NO₂ VCDs retrieved from GeoTASO within 0.5 km and 30 min with NO₂ concentrations obtained from Air-Korea.

2.4 GeoTASO measurements

NO₂ VCDs were retrieved from the L1B radiance dataset (version: V02y) obtained using GeoTASO during the KORUS-AQ campaign. The NASA Goddard Space Flight Center conducted the L1B radiance calibration, which included offset and smear correction, gain matching, amplifier cross-talk correction, dark rate correction, integration normalisation, sensitivity derivation, wavelength registration, geo-registration, non-linearity correction, and ground pixel geolocation (Kowalewski et al., 2017; Chong et al., 2020). The detailed specifications of GeoTASO are listed in Table 1.

Table 1. Summary for GeoTASO instrument and optical specification.

L1B version	V02y
Cross-track field of view	45°
Wavelength	UV: 290–400 nm VIS: 415–695 nm
Spectral resolution (full width at half maximum, FWHM)	UV: ~0.39 nm VIS: ~0.88 nm
CCD	1,056 (wavelength) × 1,033 (cross-track)
Spatial resolution before binning	~35 m (along-track) × 7 m (cross-track)

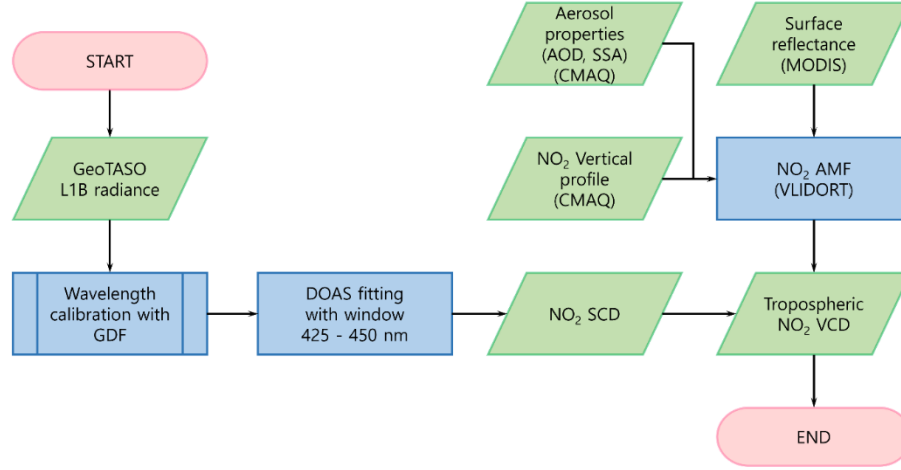


Figure 2. Flowchart of the algorithm for retrieving tropospheric NO₂ data from GeoTASO.

2.4.1 NO₂ slant column density retrieval

Figure 2 shows the flowchart for retrieving the tropospheric NO₂ VCD from the GeoTASO. We first retrieved NO₂ SCDs using the DOAS method (Platt, 1994). Nonlinear least square minimisation was used to retrieve the NO₂ SCDs which minimize the difference between the measured optical depth and the modelled value in QDOAS software (Eq. (1); Danckaert et al., 2012).

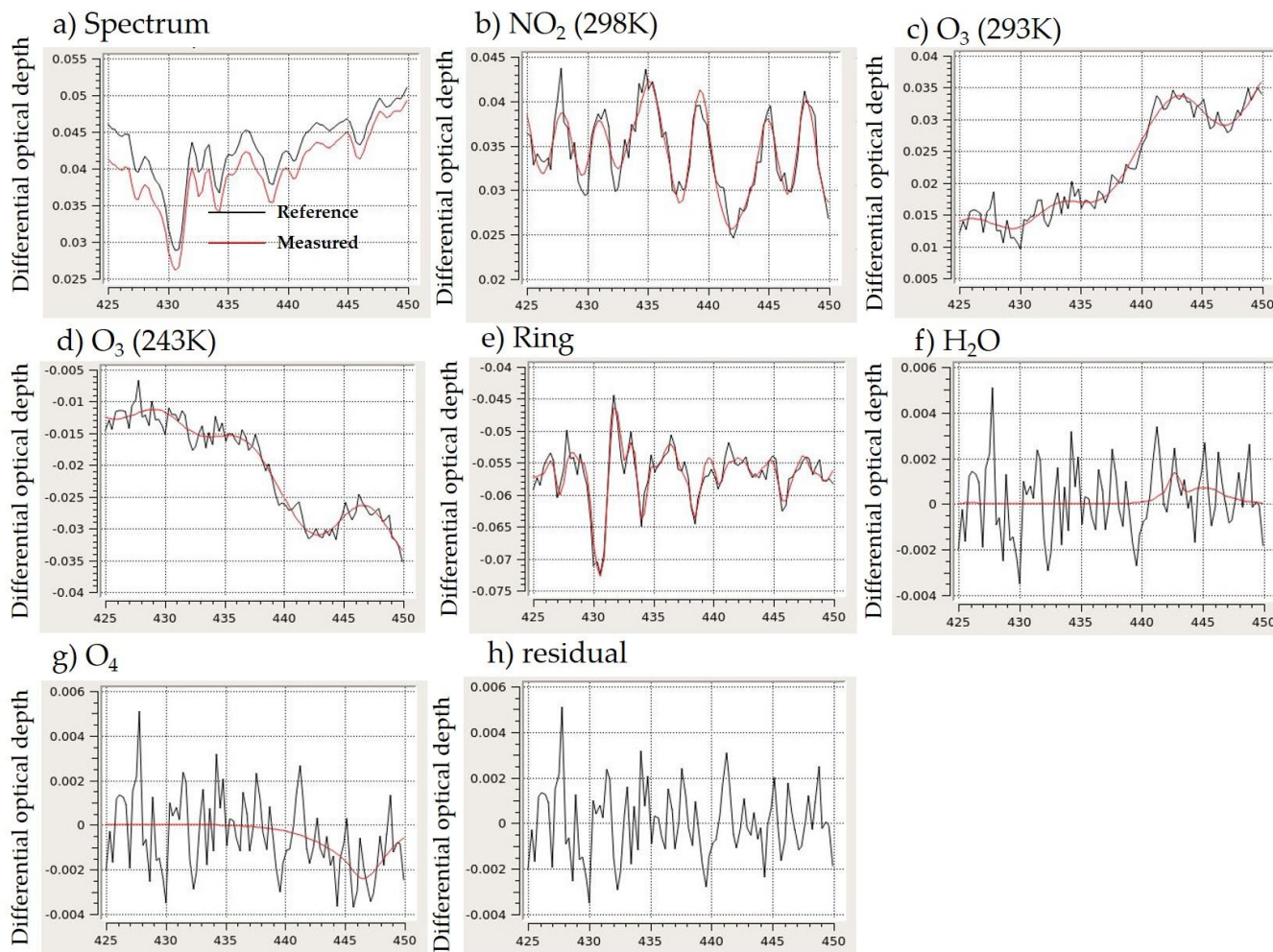
$$\frac{\ln I(\lambda)}{\ln I_0(\lambda)} = -(\sum_{j=1}^m \rho_j \times \sigma'_j(\lambda) + B(\lambda) + R(\lambda) + A(\lambda) + N(\lambda)) \quad (1)$$

Where $I(\lambda)$ is the measured earthshine radiance at wavelength λ ; I_0 is the reference radiance from the sea surface south of Jeju Island (red circle in Fig. 1, 32.983°N, 126.392°E) on 09 AM in 1 May 2016. The Community Multiscale Air Quality (CMAQ) modelling system data indicated that the NO₂ VCD from the surface to 50 hPa at this point on this day was 6.75×10^{15} molecules cm⁻² (averaged NO₂ VCD obtained from OMI available during KOURS-AQ period is 4.77×10^{15} molecules cm⁻² and standard deviation of 1.33×10^{15} molecules cm⁻², respectively); ρ_j represents the SCD of each species j ; $\sigma'_j(\lambda)$ represents the differential gas phase absorption cross-section convolved with the Gaussian distribution function (GDF) with GeoTASO FWHM (the UV and VIS range were 0.34–0.49 nm and 0.70–1.00 nm, respectively (Nowlan et al., 2016)) at wavelength λ of

187 species j , respectively. The spectral fitting window was selected from 425 to 450 nm. To determine the wavelength registration
 188 more accurately in the narrow fitting window, additional wavelength calibration of the spectra for each of the 33 across track
 189 pixels was performed using a high-resolution solar reference spectrum (Kurucz solar spectrum) (Chance and Kurucz, 2010)
 190 with the GDF. The absorption cross-sections of NO_2 (Vandaele et al., 1998), O_3 (Bogumil et al., 2000), H_2O , and the Ring
 191 effect as pseudo-absorbers (Chance and Spurr, 1997) were used to construct the model equation; and $B(\lambda)$, $R(\lambda)$, $A(\lambda)$, and
 192 $N(\lambda)$ are the broad absorption of the trace gases, extinction by Mie and Rayleigh scattering, variation in the spectral sensitivity
 193 of the detector or spectrograph, and noise, respectively, which were accounted by an 8th order polynomial. An example of the
 194 spectral fitting results is presented in Fig. 3.

195

196



197

198 **Figure 3. An example of the spectral fitting results of NO_2 retrievals from GeoTASO during the KORUS-AQ campaign (at Gangnam,**
 199 **Seoul on 9 June, 2016). Red and black line in the panel (a) represent measured and reference spectrum, respectively. The panels**

from (b) to (h) depict examples of spectral fitting results of (b) NO₂, (c) O₃(293K), (d) O₃(243K), (e) ring, (f)H₂O, (g) O₄ where red and black lines are absorption cross section of target species and the fitting residual plus the absorption of the target species, respectively. The panel (h) shows fitting residual of this example.

203

204 2.4.2 NO₂ AMF calculation

205 AMF, the ratio of SCD to VCD, can be calculated using the scattering weight (ω) and shape factor (S) (Palmer et al., 2001) in
206 Eq. (2)–(5).

$$207 \text{ AMF} = \frac{SCD}{VCD} \quad (2)$$

$$208 \text{ AMF} = \text{AMF}_G \int_{z_1}^{z_2} \omega(z)S(z)dz \quad (3)$$

$$209 \omega(z) = - \frac{1}{\text{AMF}_G} \frac{\partial \ln I_B}{\partial \tau} \quad (4)$$

$$210 S(z) = \frac{\alpha(z)n(z)}{\int_{z_1}^{z_2} \alpha(z)n(z)dz} \quad (5)$$

211 Where AMF_G represents the geometric AMF, I_B is the earthshine radiance, τ is the optical depth, α is the absorption cross-
212 section, and n is the number density of the absorber. NO₂ AMF was calculated using a linearised pseudo-spherical scalar and
213 vector discrete ordinate radiative transfer model (VLIDORT, version 2.6; Spurr and Christi, 2014). Aerosol properties, such
214 as AOD, SSA, and *a priori* NO₂ vertical profile information, were simulated using the CMAQ, and surface reflectivity was
215 obtained from the Moderate Resolution Imaging Spectroradiometer (MODIS) (Collection 6). The surface reflectance products,
216 MOD09CMG and MYD09CMG, available at a 0.05 degree (~5.6 km) spatial resolution, provide an estimate of the surface
217 spectral reflectance including MODIS bands 1 through 7. The products were corrected for atmospheric conditions such as
218 aerosol, gasses, Rayleigh scattering. In previous studies (Lamsal et al., 2017; Nowlan et al., 2018; Judd et al., 2019; Chong et
219 al., 2020), an AMF were described for both above and below aircraft altitude is used to convert NO₂ SCDs to VCDs using Eq.
220 (6)–(8).

$$221 \text{ AMF} \uparrow = \text{AMF}_G \int_{z_A}^{z_{TOA}} \omega(z)S(z)dz \quad (6)$$

$$222 \text{ AMF} \downarrow = \text{AMF}_G \int_{z_0}^{z_A} \omega(z)S(z)dz \quad (7)$$

$$223 \text{ NO}_2 \text{ VCD} \downarrow = \frac{\text{NO}_2 \text{ SCD} - \text{AMF} \uparrow \cdot \text{NO}_2 \text{ VCD} \uparrow}{\text{AMF} \downarrow} \quad (8)$$

224 Where $\text{AMF} \uparrow$ and $\text{AMF} \downarrow$ are AMF above and below aircraft, respectively, and $\text{NO}_2 \text{ VCD} \uparrow$ represents NO₂ VCD above the
225 aircraft obtained from a chemical transport model (CTM). However, here we calculated NO₂ VCD \downarrow by dividing NO₂ SCDs
226 by $\text{AMF} \downarrow$ because stratospheric and free tropospheric NO₂ ($\text{NO}_2 \text{ VCD} \uparrow$) column densities are much lower than tropospheric
227 NO₂ column densities, especially in megacities and industrial areas (Valks et al., 2011).

228

229 2.5 Chemical model description

230 Vertical profiles from CMAQ (Byun and Ching, 1999; Byun and Schere, 2006), a CTM, were used to calculate AMFs. CMAQ
231 simulations were conducted with a horizontal resolution of 15×15 km and had 27 vertical layers from the surface to 50 hPa.
232 The meteorological fields were prepared using the advanced research Weather Research and Forecasting (WRF)-Advanced
233 Research WRF (ARW) Model (Skamarock et al., 2008). Anthropogenic emissions were generated based on the KORUS v5.0
234 model (Woo et al., 2012), and biogenic emissions were simulated using the Model of Emissions of Gases and Aerosols from
235 Nature (MEGAN v2.1; Guenther et al., 2006; 2012). Besides anthropogenic and biogenic emissions, the Fire Inventory from
236 NCAR (FINN; Wiedinmyer et al., 2006, 2011) was utilised to update the pyrogenic emission fields.

237 CMAQ AOD was calculated by integrating the aerosol extinction coefficient (Q_{ext}), which is the sum of scattering (Q_{sca}) and
238 absorption (Q_{abs}) coefficients, over all vertical layers (z) as follows:

$$239 \text{ AOD} = \int Q_{sca}(z) dz = \int \{Q_{sca}(z) + Q_{abs}(z)\} dz \quad (9)$$

$$240 Q_{abs}[\text{Mm}^{-1}] = \sum_i \sum_j \{(1 - \omega_{ij}) \cdot \beta_{ij} \cdot f_{ij}(RH) \cdot [C]_{ij}\} \quad (10)$$

$$241 Q_{sca}[\text{Mm}^{-1}] = \sum_i \sum_j \{\omega_{ij} \cdot \beta_{ij} \cdot f_{ij}(RH) \cdot [C]_{ij}\} \quad (11)$$

242 Here, ω_{ij} indicates SSA of particulate species i for the particulate mode (or size bin) j , β_{ij} denotes the mass extinction
243 efficiency, $f_{ij}(RH)$ is the hygroscopicity factor according to the relative humidity (RH), and $[C]_{ij}$ is the concentration of
244 particulate species. CMAQ SSA is defined as the ratio of the integrated Q_{sca} to AOD, and NO_2 vertical profiles were obtained
245 from NO_2 concentrations at each vertical layers by conducting CMAQ simulations. Details of the model descriptions and
246 calculations of optical properties are given in Lee et al. (2020) and Malm and Hand (2007).

247 3 Results and discussion

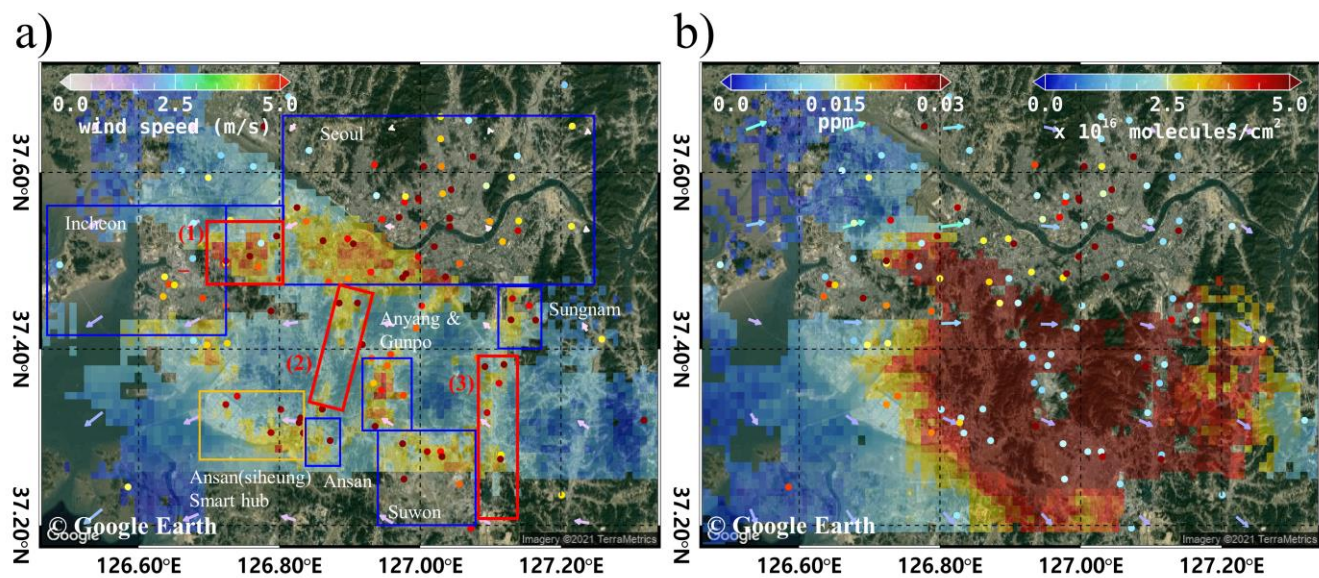
248 3.1 NO_2 VCD retrieval

249 We showed the finally NO_2 VCDs by binning them with $0.01^\circ \times 0.01^\circ$ from 250 m spatial resolution. Although the spatial
250 binning NO_2 VCDs were compared to those at native resolution, we noted that the spatiotemporal variability was still able to
251 be clearly distinguished from the background at 0.01° binning resolution. Chong et al. (2020) showed that larger VCDs at 250
252 m resolutions do not necessarily lead to larger VCDs at wider resolutions. As the results of NO_2 VCD, we selected the dates
253 observed in both the morning and afternoon during the KORUS-AQ period over Seoul metropolitan area, Busan, and Anmyeon.
254 The retrieved dates for NO_2 VCDs were 5, 9, and 10 Jun, 2016.

255 3.1.1 Seoul metropolitan region

256 The population of the Seoul metropolitan region is approximately 20 million, which is approximately 40% of the total
257 population of South Korea. It is very rare to obtain high-resolution horizontal NO_2 VCD distributions using airborne

258 measurements in the morning and afternoon, especially in Asian megacities. Fig. 4 shows tropospheric NO₂ VCDs over Seoul
 259 on 9 June 2016, at 9 AM and 3 PM local time (LT). According to the Terra/Aqua CLDMASK data (Ackerman et al., 1998),
 260 on this day, the cloud fraction was less than 0.3 over the entire domain of Fig. 4.



261 **Figure 4. Tropospheric NO₂ VCD, binned to a 0.01°×0.01° horizontal grid, in the Seoul metropolitan region on 9, June 2016 retrieved**
 262 **from GeoTASO: a) at 9 AM and b) at 3 PM. The red boxes represent expressways (counterclockwise from left to right, (1) Gyeongin**
 263 **expressway, (2) Seohaean expressway, and (3) Gyeongbu expressway), the orange box indicates the industrial complex, and the blue**
 264 **boxes indicate the major cities (Seoul, Incheon, Suwon, Bucheon, Anyang, Gunpo, Sungnam, and Ansan) of the Seoul metropolitan**
 265 **region. Colours of the circles depict the NO₂ surface mixing ratio obtained from Air-Korea. The colour arrows show the wind**
 266 **direction and speed at 1000 hPa over Seoul metropolitan region, obtained via the Unified Model (UM) simulations (background**
 267 **RGB image is from Google Earth; <https://www.google.com/maps/>).**

269
 270 In the morning, NO₂ VCDs retrieved from GeoTASO were highly correlated with expressways (red boxes in Fig. 4), such as
 271 the Gyeongin, Seohaean, and Gyeongbu Expressways, and over major cities with heavy traffic, such as Seoul, Bucheon, Ansan,
 272 Anyang, and Suwon. GeoTASO observed NO₂ VCD values three-times higher ($>3 \times 10^{16}$ molecules cm⁻²) in these areas
 273 compared to the surrounding rural areas. In particular, high NO₂ VCD values above 6×10^{16} molecules cm⁻² were observed
 274 above the Gyeongin Expressway, which has very heavy traffic in a relatively short section, and the Gunpo Complex Logistics
 275 zone, where diesel vehicle traffic is also high. The major NO₂ source regions and the regions where high NO₂ VCD values
 276 were observed were highly consistent at 9 AM because the wind speed at this time—as obtained from the unified model (UM)
 277 based Regional Data Assimilation and Prediction System (RDAPS) of the Korea Meteorological Administration (KMA)—
 278 was as low as 0.1 ms⁻¹ and the average wind direction was 84.7° at 1000 hPa over Seoul metropolitan region. The average
 279 daily traffic volume of these expressways exceeds 150,000 vehicles, and the total number of vehicles registered in these major
 280 cities is $> 6,000,000$, with an average daily mileage per car per day of over 38 km. Detailed information on these cities and

expressways is listed in Table 2 and Table 3. Based on the level of vehicular traffic, combustion using gasoline and diesel engines leads to high overall emissions of NO₂ in the Seoul metropolitan region (Kendrick et al., 2015).

Table 2. The population, number of registered vehicles, and average mileage per car per day of major cities in the Seoul metropolitan region obtained from the Korean Statistical Information Service (<https://kosis.kr/eng>).

City	Population (millions)	Vehicle registration number (thousands)	Average mileage (km/car/day)
Seoul	9.776	3,083	37.1
Incheon	2.914	1,402	41.7
Bucheon	0.848	284	37.2
Ansan	0.744	289	40.8
Anyang	0.596	206	39.6
Gunpo	0.286	87	38.8
Suwon	1.241	467	38.1
Sungnam	0.994	358	36.3

Table 3. Daily average traffic volume on the Gyeongin, Gyeongbu, and Seohaean Expressways obtained using the Traffic Monitoring System (<https://www.road.re.kr>).

Expressway	Daily average traffic volume
Gyeongin Expressway	162,369
Gyeongbu Expressway	173,413
Seohaean Expressway	150,298

Compared the data from the morning, the average wind speed and wind direction were 1.7 m/s and 284.5° at 1000 hPa in the afternoon and the afternoon had extremely high tropospheric NO₂ VCD values (exceeding 5×10^{16} molecules cm⁻²) in most of the Seoul metropolitan regions including rural areas, whereas the NO₂ mixing ratio (MR) obtained from Air-Korea decreases in the afternoon. According to Tzortziou et al. (2018), similar results were retrieved from the Pandora site in Seoul, with higher afternoon NO₂ VCDs than in the morning. This result is presumed to be due to the reason that the amount of NO₂ produced by chemical conversion of nitric oxide (NO) by O₃ and VOCs in the atmosphere, along with NO_x generated by regional emissions (traffic) in the Seoul metropolitan region, is greater than the amount lost by photolysis and transport to nearby areas (Herman

et al., 2018). In addition, the increase in tropospheric NO₂ VCD in the afternoon is presumed to be due to the accumulation and dispersion of NO₂ according to the change in the planetary boundary layer height (Ma et al., 2013).

3.1.2 Industrial and power plant regions in Anmyeon

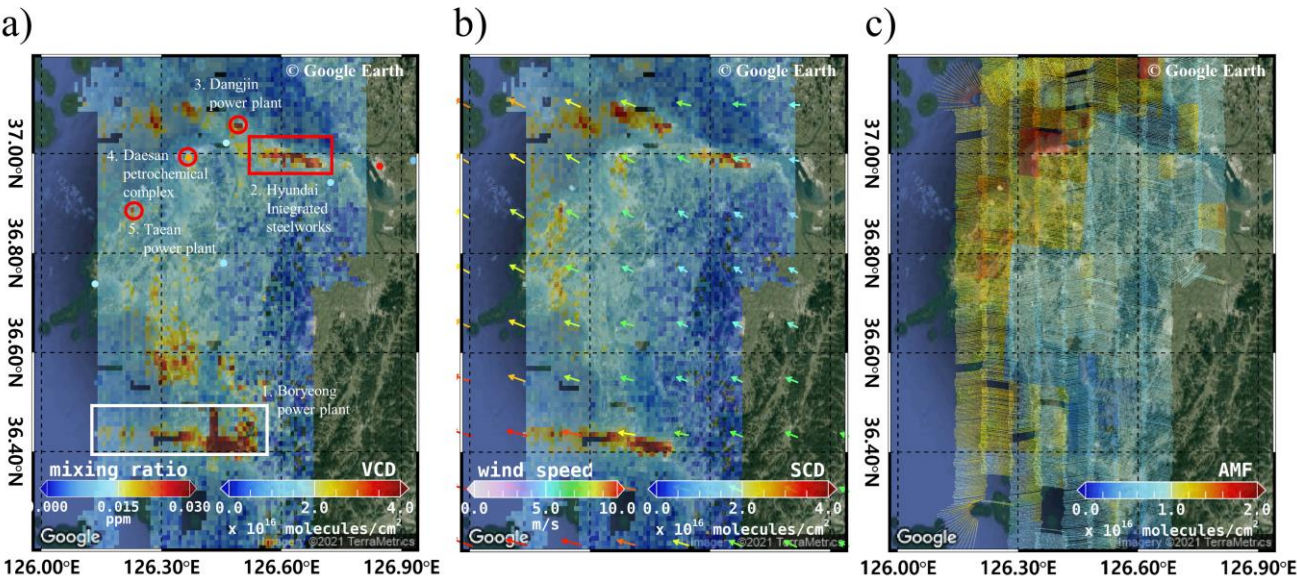


Figure 5. a) Tropospheric NO₂ VCD and b) NO₂ SCD retrieved from GeoTASO, and c) NO₂ AMF, native resolution (250 m) calculated using VLIDORT over Anmyeon in South Korea on 5 June 2016. The NO₂ VCD and SCD were gridded into a spatial resolution of 0.01°×0.01°. The colored arrows indicate wind speed and wind direction at 850 hPa from the Unified Model (UM) simulations. The red circles and rectangle in panel (a) represent the major NO₂ emission sources, such as steelworks and power plants (background RGB image is from Google Earth; <https://www.google.com/maps/>).

The high spatial resolution of tropospheric NO₂ VCD from GeoTASO over the Anmyeon industrial region, where many industrial facilities and several power plants are distributed, is shown in Fig. 5. The panels a and b of this figure show the binned tropospheric NO₂ VCD and NO₂ SCD retrieved from GeoTASO L1B data, respectively, between 13:00 and 17:00 LT on 5 June 2016. The panel c depicts the calculated AMF of NO₂ from native resolution over the domain. The GeoTASO observations clearly detected moderate and strong NO₂ emission sources over this area: (1) Boryeong power plant, (2) the Hyundai integrated steelworks, (3) Dangjin power plant, (4) the Daesan Petrochemical Complex, and (5) Taeon power plant. High NO₂ VCD values ($> 5 \times 10^{16}$ molecules cm⁻²) were observed over steel mill works, petrochemical complexes, and power plants, whereas values were comparatively low ($< 1 \times 10^{16}$ molecules cm⁻²) over small cities including Seosan, Dangjin, and Boryeong with populations of less than 0.1 million, and the Seohaean Expressway. In 2016, the annual NO_x emissions by the Hyundai steelworks and the Dangjin and Boryeong power plants were about 10.3, 11.9, and 16.8 kt year⁻¹, respectively. NO₂ emission rates from major industrial facilities in the Anmyeon region are shown in Table 4.

318

319 **Table 4. NO₂ emission rates from major industrial facilities in the Anmyeon region obtained from the Continuous Emission**
320 **Monitoring System of the Korea Environment Corporation (<https://www.stacknsky.or.kr/eng/index.html>).**

Industrial facilities	NO ₂ emission rate (2016) (kg/year)
Boryeong power plant	16,788,438
Hyundai integrated steelworks	10,271,075
Dangjin power plant	11,852,972
Daesan petrochemical complex	3,397,939
Taeon power plant	15,466,022

321

Figure 5 shows high NO₂ concentrations of major industrial facilities in the Anmyeon region, where fossil fuel combustion in factories and thermal power plants leads to high emissions (Prasad et al., 2012). Due to relatively sparse distribution over rural areas, the Air-Korea measurements did not detect the major NO₂ plume as shown in Fig. 5a. Thus, airborne remote sensing systems, such as GeoTASO, can effectively compliment the ground-based networks for monitoring minor and major NO₂ emissions, particularly over these remote industrial regions.

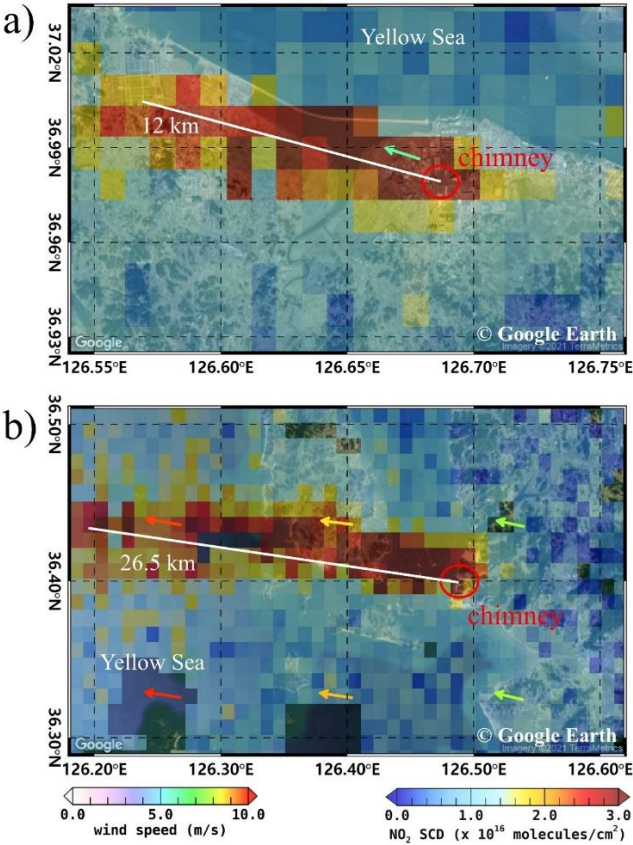


Figure 6. Enlarged view of GeoTASO tropospheric NO₂ VCD observation over a) Hyundai steel works, indicated by the red box in Figure 5, and b) the Boryeong power plant, indicated by the white box in Figure 5. The data were gridded to a spatial resolution of 0.01°×0.01°. The arrows represent the wind direction and speed at 850 hPa from the Unified Model (UM) simulations, respectively (background RGB image is from Google Earth; <https://www.google.com/maps/>).

The GeoTASO data captured not only NO₂ emissions from the chimneys of steelworks and power plants but also its transport by the wind. Fig. 6a and 6b show enlarged views of tropospheric NO₂ SCD retrieved using GeoTASO over the Hyundai steelworks (red box in Fig. 5) and the Boryeong power plant (white box in Fig. 5). The arrows in Fig. 6 represent the prevailing wind direction and speed from RDAPS. NO₂ emitted from the chimneys of these sites was transported to the Yellow Sea,

travelling distances of over 26 km at speeds of approximately 6 ms^{-1} . According to Chong et al. (2020), similar results were found for SO_2 emitted and transported from these sites.

3.1.3 Busan metropolitan region

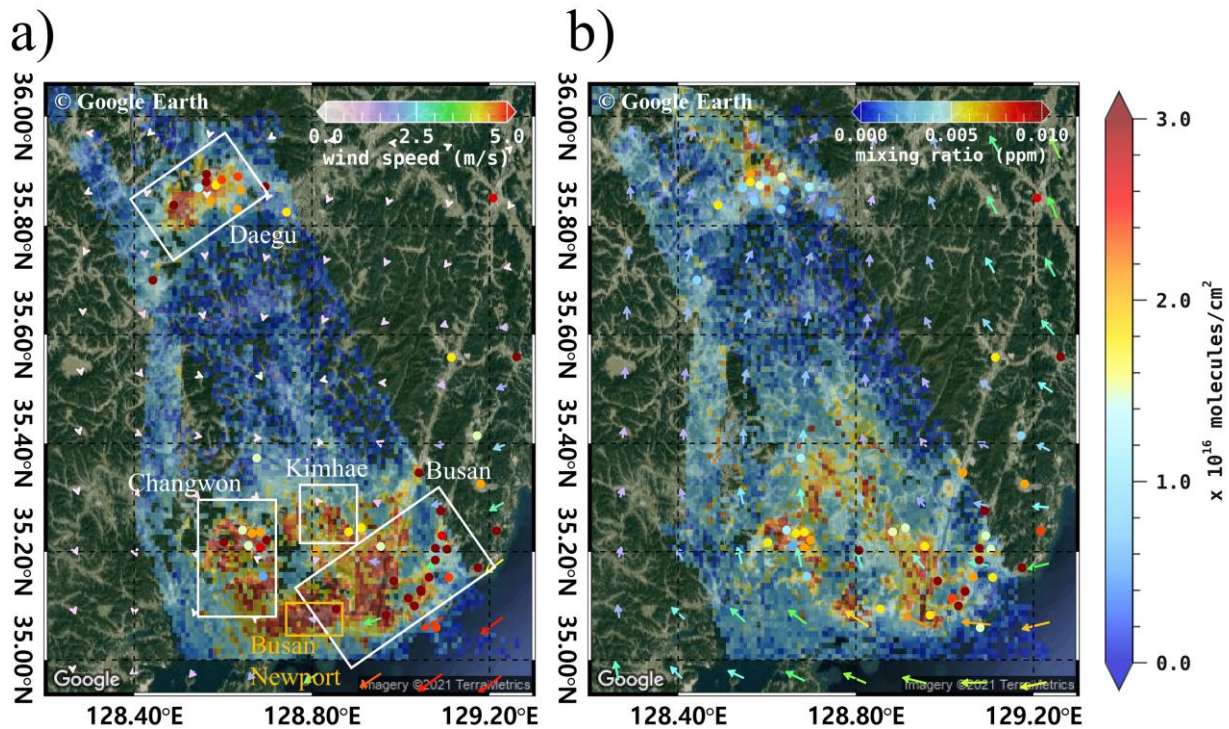


Figure 7. Tropospheric NO_2 VCD in the Busan metropolitan region in the (a) morning and (b) afternoon of 10 June 2016. The data were gridded into to a spatial resolution of $0.01^\circ \times 0.01^\circ$. The wind speed (colours scale) and wind direction (arrows) at 1000 hPa pressure level were obtained from the Unified Model (UM) simulations. The white boxes represent major cities such as Busan, Daegu, Changwon, and Kimhae. The orange box represents Busan Newport (background RGB image is from Google Earth; <https://www.google.com/maps/>).

Fig. 7a and 7b show tropospheric NO_2 VCD retrieved from the GeoTASO L1B data over the Busan metropolitan region on 10 June 2016 in the morning (between 08:00 and 11:00 LT) and afternoon (between 13:00 and 16:00 LT), respectively. The arrows in Fig. 7 show the wind speed and wind direction of 1000 hPa obtained from the UM-RDAPS, with the average wind speed and wind direction of 0.9 m/s and 55.4° , 1.9 m/s and 147.0° , respectively, in the morning and afternoon. High NO_2 VCDs were observed above urban areas, the port, industrial complexes, and the inter-city road between Busan and Changwon. Similar to the Seoul metropolitan regions, it is estimated that combustion using gasoline and diesel engines contributes to the high NO_2 emission. In the morning, NO_2 VCDs were high (approximately $3 \times 10^{16} \text{ molecules cm}^{-2}$) in the major cities and, especially, around Busan Newport, with values exceeding $7 \times 10^{16} \text{ molecules cm}^{-2}$. In comparison, in the mountainous regions

355 between Daegu and Busan, NO₂ VCD values were less than 1×10^{16} molecules cm⁻² during the same period. The spatial
356 distribution of tropospheric NO₂ VCDs was similar to that in the Seoul metropolitan regions, with high values over major cities
357 and roads (compare Figs. 4 and 7). In Busan, fossil fuel combustion using both road vehicles and ships likely contributes to
358 the NO₂ emissions. In the afternoon, unlike Seoul metropolitan region, tropospheric NO₂ VCD over Busan decreased by over
359 3×10^{16} molecules cm⁻², which also corresponds with NO₂ MR data obtained from the Air-Korea sites. Detailed information
360 on these cities is listed in Table 5.

361

362 **Table 5. The population, number of registered vehicles, and average mileage per car per day of major cities in the Busan**
363 **metropolitan region obtained from the Korean Statistical Information Service (<https://kosis.kr/eng>).**

City	Population (millions)	Vehicle registration number (thousands)	Average mileage (km/car/day)
Busan	3.389	1,295	40.1
Daegu	2.450	1,121	37.1
Changwon	1.080	551	37.5
Kimhae	0.529	250	38.0

364

365 3.2 Error estimation

366 NO₂ VCD retrieval accuracy using the DOAS method depends on both the AMF calculation and spectral fitting error of the
367 SCD retrieval. Retrieval errors of the NO₂ VCD were estimated using error propagation analysis as expressed in Eq. (12).

$$368 \frac{\varepsilon_{VCD}}{VCD} = \sqrt{\left(\frac{\varepsilon_{SCD}}{SCD}\right)^2 + \left(\frac{\varepsilon_{AMF}}{AMF}\right)^2} \quad (12)$$

369 Where ε_{VCD} is the total error of NO₂ VCD. The error of NO₂ SCD (ε_{SCD}) is obtained from the spectral fitting error of NO₂ SCD
370 via DOAS spectral fitting. ε_{AMF} indicates the error of NO₂ AMF caused by uncertainties in the model input parameters for
371 AMF calculation. Uncertainties in aerosol properties (AOD, SSA, and ALH) and surface reflectance for the RTM calculations
372 are known to be the major factors affecting NO₂ AMF accuracy (Boersma et al., 2004; Leitão et al., 2010; Hong et al., 2017).
373 Therefore, in this present study, we quantified the NO₂ AMF errors (ε_{AMF}) due to uncertainties in the input parameters
374 independent of one another using Eq. (13):

$$375 \varepsilon_{AMF} = \sqrt{\left(\frac{\partial AMF}{\partial AOD}\right)^2 \sigma_{AOD}^2 + \left(\frac{\partial AMF}{\partial SSA}\right)^2 \sigma_{SSA}^2 + \left(\frac{\partial AMF}{\partial ALH}\right)^2 \sigma_{ALH}^2 + \left(\frac{\partial AMF}{\partial SFR}\right)^2 \sigma_{SFR}^2} = \sqrt{\sum_{i=1}^4 \left(\frac{\partial AMF}{\partial \chi_i}\right)^2 \sigma_{\chi_i}^2}, \quad (13)$$

376 where $\frac{\partial AMF}{\partial \chi_i}$ are partial derivatives of NO₂ AMF with respect to the input parameters (χ_i), σ_{χ_i} represents the uncertainty of the

377 χ_i . The σ of AOD, SSA, surface reflectance, and ALH are assumed as 30% (Ahn et al., 2014), 0.04 (Jethva et al., 2014),
378 (0.005+0.05×surface reflectance; EOS Land Validation; <https://landval.gsfc.nasa.gov>), and 1 km (Fishman et al., 2012),

379 respectively, in this study. To derive $(\frac{\partial AMF}{\partial \chi_i})^2$, the true χ_i is input to the RTM to simulate ‘true’ NO₂ AMF. For the AOD, SSA,
 380 ALH, and surface reflectance (SFR), perturbed NO₂ AMF was simulated using RTM with $\chi_i \pm \sigma_{\chi_i}$. $\partial \chi_i$ denotes the difference
 381 between the ‘true’ χ_i and $\chi_i \pm \sigma_{\chi_i}$, and ∂AMF is the difference between the ‘true’ NO₂ AMF (AMF_{true}) simulated with ‘true’
 382 input values and the new NO₂ AMF (AMF_{new}) simulated using the perturbed input parameters $\chi_i \pm \sigma_{\chi_i}$ (i.e. the original input
 383 parameters modified by the uncertainty). The simulation for calculating the ε_{AMF} was conducted using the input parameters
 384 on 9 June 2016. On the flight day, average (standard deviation) values of AOD, SSA, ALH, and surface reflectance were 0.39
 385 (0.10), 0.98 (0.001), 0.27 km (0.10 km), and 0.09 (0.04), respectively.

387 **Table 6. Total errors of NO₂ VCD caused by uncertainties in NO₂ SCD and NO₂ AMF (the average for the flight on 9 June**
 388 **2016).**

NO ₂ AMF errors	AOD	3.0%
	SSA	4.2%
	aerosol loading height	26.4%
	surface reflectance	2.8%
	total NO₂ AMF error due to aerosol uncertainties	27.8%
NO ₂ SCD error		11.9%
NO₂ VCD error		31.1%

389
 390 Table 6 lists the estimated NO₂ VCD error on 9 June 2016 for each sources based on the error propagation method. The error
 391 estimation was conducted for the pixels where root mean square residual < 0.001 and NO₂ VCD > 5 × 10¹⁵ molecules cm⁻²
 392 since NO₂ SCD precision is reported to be highly decreased in low NO₂ conditions (Hong et al., 2017). The total NO₂ VCD
 393 error was 31.1% with a high portion of NO₂ AMF error. The NO₂ SCD error was calculated to be 11.9%, showing the
 394 importance of accurate DOAS spectral fitting to derive NO₂ SCD. The total AMF error due to uncertainties in input parameters
 395 was calculated to be 27.8%. Among model input parameters, the effect of ALH on NO₂ AMF become highest (26.4%),
 396 indicating importance of accurate aerosol profile information. ALH sensitively affects NO₂ AMF because near the surface
 397 where trace gases and aerosols are well mixed, aerosols lead to multiple scattering effects and the light absorption of trace
 398 gases due to increasing light path (Castellanos et al., 2015; Hong et al., 2017). Especially, ALH can be the most important
 399 input parameter in the Asia region where high loadings of aerosol plumes persist throughout the year. The NO₂ AMF

400 calculation errors due to uncertainties in SSA and AOD were 4.2% and 3.0%, respectively. The NO₂ AMF calculation error
 401 due to uncertainties in aerosol optical properties (SSA and AOD) seems smaller than those in the previous study (Leitão et al.,
 402 2010). The smaller effect of aerosol properties can be explained by the moderate aerosol loading (AOD = 0.39) on the flight
 403 day. It is expected that NO₂ AMF errors become larger under high AOD condition. The smallest effect of SRF was found on
 404 NO₂ AMF calculation error. A priori NO₂ profile shape also can be one of factors to cause calculation error for NO₂ AMF as
 405 reported in the previous studies (Leitao et al., 2010, Meier et al., 2016). It is necessary to calculate the effect of a priori NO₂
 406 profile shape on airborne NO₂ AMF error in the future. Moreover, the resulting uncertainties of input parameters of a
 407 GeoTASO ground pixel need to be considered by combining the initial uncertainties of CTM and satellite-based products, and
 408 by the variability of the parameters within a grid box. This kind of analysis should be taken into account in further study.

$$409 \quad AMF_{percent_diff} = \frac{\partial AMF}{(AMF_{true} + AMF_{new}) \div 2} \times 100 \quad (14)$$

410

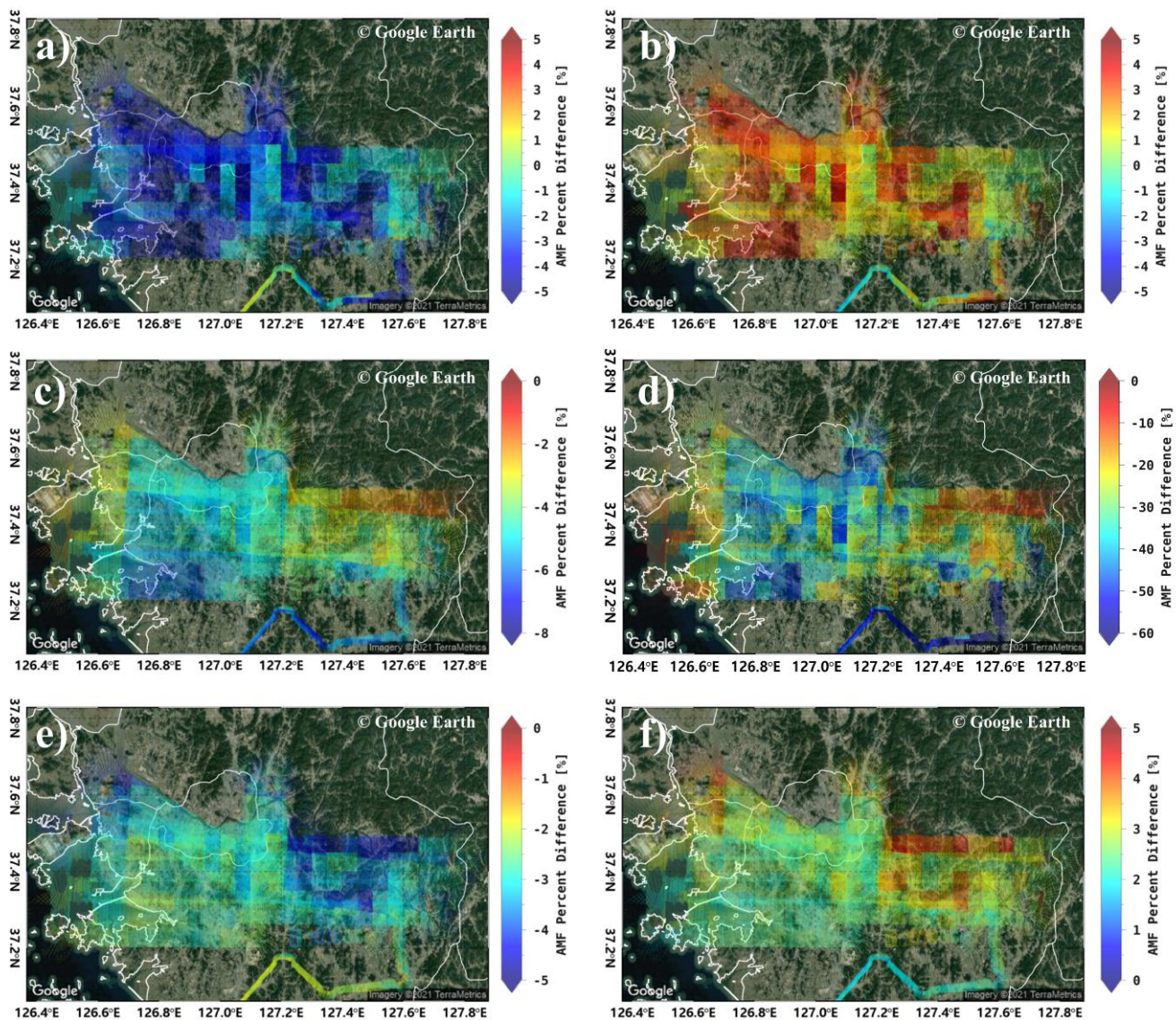


Figure 8. Percentage difference between AMF calculated using the CMAQ model simulation and those using a) 30% lower AOD, b) 30% higher AOD, c) 0.04 lower SSA, d) 1km higher ALH, compared to the model outputs. The percentage difference for AMF calculated using MODIS data and those using e) 20% $0.005 + 0.05 \times \text{SFR}$ lower SFR, f) $0.005 + 0.05 \times \text{SFR}$ higher SFR (background RGB image is from Google Earth; <https://www.google.com/maps/>).

In this present study, we additionally investigated the spatial distribution of AMF calculation errors associated with uncertainties in aerosol properties (AOD, SSA, ALH, and SFR). Percent difference of NO_2 AMF ($\text{AMF}_{\text{percent_diff}}$) was calculated on each spatial pixel using Eq. (14). Fig. 8a and 8b show the percent difference error between the calculated AMFs using the

420 CMAQ AOD data with 30% lower (Fig. 8a) and 30% higher (Fig. 8b) values, respectively. The AMF decreased and increase
 421 by up to 7% with decreasing and increasing AOD, respectively, in the Seoul metropolitan region. We estimated that, under
 422 low aerosol loading conditions, an increase in AOD near the surface leads to an increase in the scattering probability within
 423 the surface layer with high NO₂ concentrations. Fig. 8c shows the percent difference error between the calculated AMFs using
 424 CMAQ SSA data with a 0.04 lower value. The AMF decreased with decreasing SSA because the absorption of light increased.
 425 The ALH was also found to highly affect the accuracy of the AMF calculations (Fig. 8d). The ALH uncertainty of 1 km
 426 decreased AMFs with average AMF_{percent_diff} of -27% on the flight day. Especially, on the pixels where AOD > 0.6, the average
 427 AMF_{percent_diff} was found to be -37% while that was -23% on the pixels where AOD < 0.4, showing the combined effect of
 428 aerosol loading and aerosol profile shape on the NO₂ AMF calculations. Fig. 8e and 8f show the percentage difference error
 429 between the calculated AMFs using the MODIS surface reflectance data with $0.005 + 0.05 \times \text{SFR}$ lower (Fig. 8e) and $0.005 +$
 430 $0.05 \times \text{SFR}$ higher (Fig. 8f) values, respectively. The AMF decreased by about 6% when surface reflectance decrease, and vice
 431 versa when it increased.

432 3.3 Validation of NO₂ VCDs retrieved from GeoTASO

433 Tropospheric NO₂ VCDs retrieved from GeoTASO L1B data (NO_{2,G}) were compared with those obtained from OMI NO₂
 434 VCDs (NO_{2,O}) and Pandora (NO_{2,P}). The NO_{2,O} were only available for 10 June during the campaign period. Therefore, we
 435 only compared 37 NO_{2,G} and NO_{2,O} data points within a radius of 20 km and 30 min, which yielded a correlation coefficient
 436 of 0.70 with a slope of 0.41 (Fig. 9 a)). In order to validate, All NO_{2,G} within a radius 20 km of the OMI center coordinate were
 437 averaged.
 438 The NO₂ values are relatively low since GeoTAOS observation is carried out in a region with low NO₂ compared to Seoul
 439 metropolitan and the overpass time of OMI is about 13:30 LT when NO₂ decreased. It is thought that the reson the low slope
 440 value is because the OMI with low spatial resolution does not reflect the spatial NO₂ inhomogeneity in the pixel.

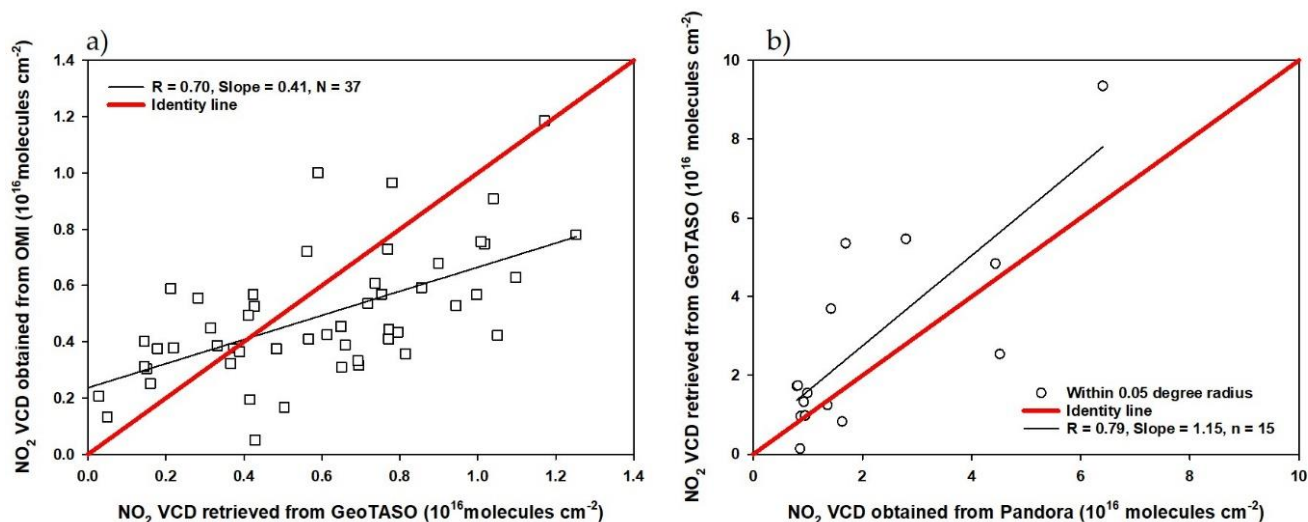


Figure 9. Scatter plots of a) NO₂ VCD retrieved from GeoTASO and those obtained from OMI and b) NO₂ VCD obtained from Pandora and those retrieved from GeoTASO, respectively.

To validate the accuracy of NO_{2,G} data, we made a comparison with NO₂ VCD obtained from the Pandora system (NO_{2,P}) during the KORUS-AQ campaign period. NO_{2,P} obtained from Busan University, Olympic Park, Songchon, Yeosu, and Yonsei University Pandora sites on June 5, 9, and 10 were used for the GeoTASO validation (Fig. 1). NO_{2,G} and NO_{2,P} columns at these sites are compared in Fig. 10. In order to compare NO_{2,G} and NO_{2,P}, we used averaged NO_{2,G} retrieved from 16 across track with smallest viewing zenith angle and averaged 30 min NO₂ obtained from Pandora measurement within a radius of 0.05 degree. NO_{2,G} and NO_{2,P} were correlated (R = 0.79, with a slope of 1.15), however, when NO_{2,P} was lower than 1×10^{16} molecules cm⁻², the correlation coefficient between NO_{2,G} and NO_{2,P} was < 0.1. The weak correlation at low NO₂ levels are most likely to reflect the differences in viewing geometries and the horizontal inhomogeneity of the measured NO₂ between Pandora and GeoTASO. Also, from this result, it is thought that it can be used for NO₂ validation of geostationary satellite such as GEMS using Pandora and GeoTASO. However, since the number of Pandora is limited in this campaign, we had difficulties to validate NO₂ retrieved from GeoTASO under various conditions. I believe that many ground-based remote sensing measurements are needed to validate GEMS under various conditions.

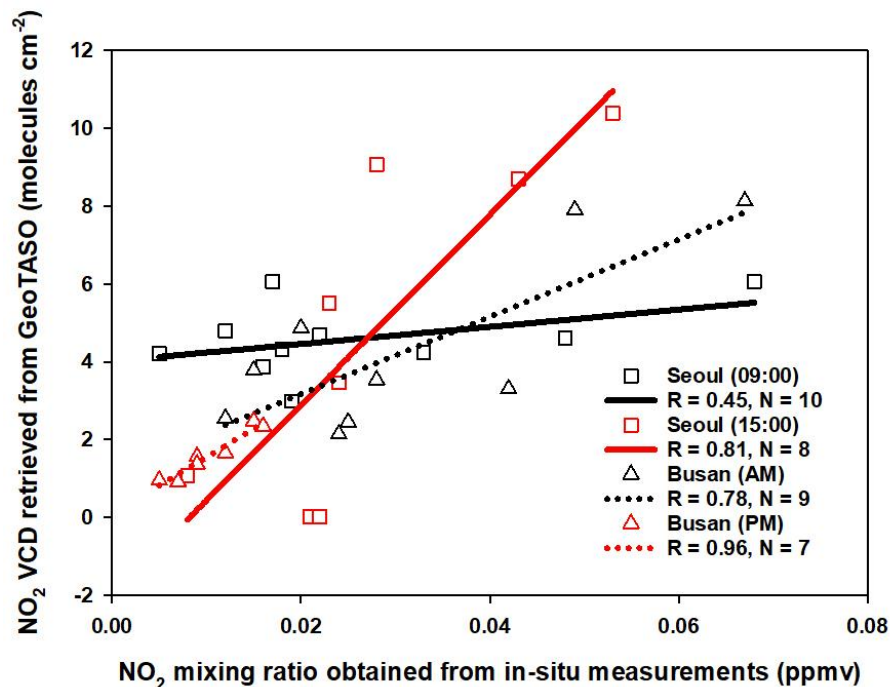


Figure 10. Scatter plot of the NO₂ VCDs retrieved from GeoTASO, and NO₂ surface mixing ratio obtained from Air-Korea. The black and red squares represent the NO₂ data at 9 AM and 3 PM (local time) over the Seoul metropolitan region, respectively. The black and red triangles represent those in the morning and afternoon, over Busan, respectively.

To evaluate the spatiotemporal distribution of NO₂ VCDs retrieved from GeoTASO, NO_{2,G} in comparisons to surface spatial patterns, NO_{2,G} was compared with NO_{2,A} for GeoTASO data within a radius of approximately 0.05 km and 30 min (Fig. 9). In order to compare NO_{2,G} and NO_{2,A}, we used averaged NO_{2,G} retrieved from 16 across track and averaged 30 min within a radius of 0.05 degree. Since in-situ measurements provides NO₂ VMR (NO_{2,A})(ppmv) once per hour, NO_{2,A} of the nearest time is used to compare with NO_{2,G}. The correlation coefficient (R) between NO_{2,G} (molecules cm⁻²) and NO_{2,A} at 9 AM and 3 PM LT in the Seoul metropolitan region was 0.45 and 0.81, respectively. When using only roadside station data from Air-Korea, the R-value for the morning increased to 0.83, which implies GeoTASO is more sensitive to emissions from NO₂ source areas, such as roadsides. As a result of the comparison, there were large differences in the morning and afternoon. These results were identified because synoptic meteorology played an important role from June 1 to June 10, 2016 (Choi et al., 2019). As described by Judd et al. (2018), the spatial distribution for NO₂ VCDs appears that reflects the emission source in local industrialized regions and transportations in the morning with relatively weak winds. In general, NO₂ concentration increases to late morning, indicating that the emissions process proceeds faster than the NO₂ removal process. As the planetary boundary layer heights (PBLH) in early afternoon increase and surface NO₂ is mixed through a deeper PBLH, the NO₂ VCDs distribution showed a wider increase in most of the Seoul metropolitan area and the overall column amounts continue to increase (Judd et al., 2018).

480 In addition, when comparing NO₂ VCDs with surface NO₂ concentrations, it should be interpreted carefully that it is a non-
481 linear relationship between NO_{2,G} and NO_{2,A}. Although it may vary depending on weather conditions, high NO₂ VCDs from
482 airborne observations may sometimes be detected with low surface NO₂ concentrations. In particular, when exhaust gases
483 emitted from industrial facilities are happen at a certain altitude (stacks/chimneys), NO_{2,G} show high NO₂ VCDs, but NO_{2,A}
484 may be observed to have a low concentration. Unfortunately, in Anmyeon industrial region, NO_{2,G} and NO_{2,A} could not be
485 compared due to spatial restrictions because the distribution of ground observation stations is concentrated in metropolitan
486 areas.

487 In the Busan metropolitan area, the R-value of the NO_{2,G} and NO_{2,A} data had a correlation coefficient greater than 0.78. This
488 reflects the more even horizontal distribution of NO₂ in the afternoon, when diffusion from the source areas had taken place.
489 However, for a more accurate comparison, NO₂ VCD data should be converted to NO₂ MR based on mixing layer height,
490 temperature, and pressure profile data (Kim et al., 2017; Qin et al., 2017; Jeong and Hong, 2021a). However, since the number
491 of pandora and satellite data is limited in this campaign, we had difficulties to validate NO₂ retrieved from GeoTASO under
492 various conditions. Since ground-based, airborne and space borne remote sensing measurements has their own advantage and
493 disadvantage, I believe that a comprehensive observation campaign involving all of groud-based, airborne and space borne
494 measurements should be carried out continuously for upcoming new era of geostationary environmental satellite.

495 4 Conclusions

496 For the first time, we have retrieved NO₂ VCD data using airborne GeoTASO observations over the Seoul metropolitan
497 region—one of the most populous cities worldwide, the Busan metropolitan region—the second-largest city in South Korea,
498 and Anmyeon, with thermal power plants and industrial complexes. By retrieving NO₂ data using GeoTASO L1B radiance, it
499 was possible to observe the spatial distribution of NO₂ over these metropolitan and industrial regions. In the morning,
500 tropospheric NO₂ VCD over Seoul showed a strong horizontal gradient between rural and urban areas. In urban areas,
501 tropospheric NO₂ VCD was high, with values exceeding 3×10^{16} molecules cm⁻²; in rural areas, values were typically below
502 1×10^{16} molecules cm⁻². Extremely high values over 10×10^{16} molecules cm⁻² were also observed in both rural and urban
503 areas. In Anmyeon, GeoTASO observations showed NO₂ is mainly emitted from the chimneys of industrial complexes and
504 thermal power plants, and subsequently transported by wind approximately 30 km to the Yellow Sea of the west coast of the
505 Korean Peninsula. In the Busan metropolitan region, in the morning, tropospheric NO₂ VCDs showed a similar pattern to the
506 Seoul metropolitan region, with high values above the inter-city road. However, in contrast to Seoul, tropospheric NO₂ VCDs
507 in Busan decreased in the afternoon due to different weather conditions locally.

508 To compare the data retrieved from the GeoTASO system, we compared NO_{2,G} with NO_{2,O} obtained from the OMI, NO_{2,A}
509 obtained from Air-Korea, and NO_{2,P} obtained from the Pandora observation system. When the distance between two
510 observations was below 20 km or 0.05 degree within 30 min, the correlation coefficients were relatively high (R = 0.70, and

79, respectively). However, the correlation between $\text{NO}_{2,G}$ and $\text{NO}_{2,A}$ over the Seoul metropolitan region was weak ($R = 0.45$) in the morning because of the more pronounced NO_2 horizontal gradient. The GeoTASO system successfully observed NO_2 VCDs with a high horizontal spatial resolution for both metropolitan and industrial regions. This demonstrates that airborne remote sensing measurements from GeoTASO, similar to GCAS, APEX and others, can be a very effective tool for the validation of trace gases retrieved from environmental satellites, including the OMI, TROPOMI, and GOME-2; these systems can obtain high-resolution measurements over relatively wide areas. However, to validate geostationary environmental satellites with higher spatiotemporal resolutions, such as the GEMS, TEMPO, and sentinel-4, additional validation strategies are needed. Based on error estimation, it can be concluded that aerosol properties are relevant and should be determined and NO_2 vertical profile retrieval performed using, for example, LIDAR, MAX-DOAS, and sondes. This is important because the accuracy of aerosol properties and the NO_2 vertical profiles affects the accuracy of AMF calculations (Leitão et al., 2010; Hong et al., 2017; Lorente et al., 2017; Boersma et al., 2018). Furthermore, as we observed in the Seoul metropolitan area, more closely spaced observations using ground-based remote sensing systems and in situ measurements are needed as NO_2 displays large horizontal gradients, especially in the morning.

Author contributions

GH and HH designed and implemented the research. KL provided the CTM data. GH developed the code for model running and performed the RTM simulations. HH and UJ contributed to the analysis of ground-based data. GH and WC carried out the sensitivity test. GH, KL, HH, UJ, WC, and JJS revised and edited the paper. HH and UJ provided constructive comments. All authors contributed to this works.

Competing interests

The authors declare that they have no conflict of interest.

Acknowledgements

Pandora data were obtained from the KORUS-AQ home pages of NASA's Goddard Space Flight Center (<https://avdc.gsfc.nasa.gov/pub/DSCOVr/Pandora/DATA/KORUS-AQ/>). Ground-based NO_2 MR data were obtained from Air-Korea (http://www.airkorea.or.kr/web/detailViewDown?pMENU_NO=125/). The authors would like to thank KORUS-AQ campaign team for providing the GeoTASO and Pandora data.

536 **Funding**

537 This work was funded by the National Institute of Environmental Research (NIER) of Ministry of Environment [No. NIER-
538 2021-01-01-100].

539 **References**

- 540 Ackerman, S. A., Strabala, K. I., Menzel, W. P., Frey, R. A., Moeller, C. C., and Gumley, L. E.: Discriminating clear sky from
541 clouds with MODIS, *J. Geophys. Res.*, 103, 32141–32157, <https://doi.org/10.1029/1998JD200032>, 1998.
- 542 Boersma, K. F., Eskes, H. J., and Brinksma, E. J.: Error analysis for tropospheric NO₂ retrieval from space: ERROR
543 ANALYSIS FOR TROPOSPHERIC NO₂, *J. Geophys. Res.*, 109, n/a-n/a, <https://doi.org/10.1029/2003JD003962>, 2004.
- 544 Boersma, K. F., Eskes, H. J., Richter, A., De Smedt, I., Lorente, A., Beirle, S., van Geffen, J. H. G. M., Zara, M., Peters, E.,
545 Van Roozendaal, M., Wagner, T., Maasakkers, J. D., van der A, R. J., Nightingale, J., De Rudder, A., Irie, H., Pinardi, G.,
546 Lambert, J.-C., and Compernelle, S. C.: Improving algorithms and uncertainty estimates for satellite NO₂ retrievals: results
547 from the quality assurance for the essential climate variables (QA4ECV) project, *Atmos. Meas. Tech.*, 11, 6651–6678,
548 <https://doi.org/10.5194/amt-11-6651-2018>, 2018.
- 549 Brauer, M., Hoek, G., Van Vliet, P., Meliefste, K., Fischer, P. H., Wijga, A., Koopman, L. P., Neijens, H. J., Gerritsen, J.,
550 Kerkhof, M., Heinrich, J., Bellander, T., and Brunekreef, B.: Air Pollution from Traffic and the Development of Respiratory
551 Infections and Asthmatic and Allergic Symptoms in Children, *Am J Respir Crit Care Med*, 166, 1092–1098,
552 <https://doi.org/10.1164/rccm.200108-007OC>, 2002.
- 553 Burrows, J. P., Hölzle, E., Goede, A. P. H., Visser, H., and Fricke, W.: SCIAMACHY—scanning imaging absorption
554 spectrometer for atmospheric chartography, *Acta Astronautica*, 35, 445–451, [https://doi.org/10.1016/0094-5765\(94\)00278-T](https://doi.org/10.1016/0094-5765(94)00278-T),
555 1995.
- 556 Burrows, J. P., Weber, M., Buchwitz, M., Rozanov, V., Ladstätter-Weißenmayer, A., Richter, A., DeBeek, R., Hoogen, R.,
557 Bramstedt, K., Eichmann, K.-U., Eisinger, M., and Perner, D.: The Global Ozone Monitoring Experiment (GOME): Mission
558 Concept and First Scientific Results, 56, 151–175, [https://doi.org/10.1175/1520-0469\(1999\)056<0151:TGOMEG>2.0.CO;2](https://doi.org/10.1175/1520-0469(1999)056<0151:TGOMEG>2.0.CO;2),
559 1999.
- 560 BYUN, D.: Science algorithms of the EPA Models-3 Community Multiscale Air Quality (CMAQ) Modeling System, 1999.
- 561 Byun, D. and Schere, K. L.: Review of the Governing Equations, Computational Algorithms, and Other Components of the
562 Models-3 Community Multiscale Air Quality (CMAQ) Modeling System, *Appl. Mech. Rev.*, 59, 51,
563 <https://doi.org/10.1115/1.2128636>, 2006.
- 564 Callies, J., Corpaccioli, E., Eisinger, M., Hahne, A., and Lefebvre, A.: GOME-2-Metop’s second-generation sensor for
565 operational ozone monitoring, *ESA Bull*, 1, 28–36, 2000.
- 566 Castellanos, P., Boersma, K. F., Torres, O., and de Haan, J. F.: OMI tropospheric NO₂ air mass factors over South America:
567 effects of biomass burning aerosols, *Atmos. Meas. Tech.*, 8, 3831–3849, <https://doi.org/10.5194/amt-8-3831-2015>, 2015.

568 Chance, K. and Kurucz, R. L.: An improved high-resolution solar reference spectrum for earth's atmosphere measurements in
 569 the ultraviolet, visible, and near infrared, *Journal of Quantitative Spectroscopy and Radiative Transfer*, 111, 1289–1295,
 570 <https://doi.org/10.1016/j.jqsrt.2010.01.036>, 2010.

571 Chance, K. V. and Spurr, R. J. D.: Ring effect studies: Rayleigh scattering, including molecular parameters for rotational
 572 Raman scattering, and the Fraunhofer spectrum, *Appl. Opt.*, 36, 5224, <https://doi.org/10.1364/AO.36.005224>, 1997.

573 Choi, S., Lamsal, L. N., Follette-Cook, M., Joiner, J., Krotkov, N. A., Swartz, W. H., Pickering, K. E., Loughner, C. P., Appel,
 574 W., Pfister, G., Saide, P. E., Cohen, R. C., Weinheimer, A. J., and Herman, J. R.: Assessment of NO₂ observations during
 575 DISCOVER-AQ and KORUS-AQ field campaigns, *Atmos. Meas. Tech.*, 13, 2523–2546, [https://doi.org/10.5194/amt-13-](https://doi.org/10.5194/amt-13-2523-2020)
 576 2523-2020, 2020.

577 Choi, W. J.: Introducing the geostationary environment monitoring spectrometer, *J. Appl. Rem. Sens.*, 12, 1,
 578 <https://doi.org/10.1117/1.JRS.12.044005>, 2018.

579 Choi, M., Lim, H., Kim, J., Lee, S., Eck, T. F., Holben, B. N., Garay, M. J., Hyer, E. J., Saide, P. E., and Liu, H.: Validation,
 580 comparison, and integration of GOCI, AHI, MODIS, MISR, and VIIRS aerosol optical depth over East Asia during the 2016
 581 KORUS-AQ campaign, *Atmospheric Measurement Techniques*, 12(8), 4619–4641, <https://doi.org/10.5194/amt-12-4619-2019>,
 582 2019.

583 Chong, H., Lee, S., Kim, J., Jeong, U., Li, C., Krotkov, N. A., Nowlan, C. R., Al-Saadi, J. A., Janz, S. J., Kowalewski, M. G.,
 584 Ahn, M.-H., Kang, M., Joiner, J., Haffner, D. P., Hu, L., Castellanos, P., Huey, L. G., Choi, M., Song, C. H., Han, K. M., and
 585 Koo, J.-H.: High-resolution mapping of SO₂ using airborne observations from the GeoTASO instrument during the KORUS-
 586 AQ field study: PCA-based vertical column retrievals, *Remote Sensing of Environment*, 241, 111725,
 587 <https://doi.org/10.1016/j.rse.2020.111725>, 2020.

588 Choo, G.-H., Seo, J., Yoon, J., Kim, D.-R., and Lee, D.-W.: Analysis of long-term (2005–2018) trends in tropospheric NO₂
 589 percentiles over Northeast Asia, *Atmospheric Pollution Research*, 11, 1429–1440, <https://doi.org/10.1016/j.apr.2020.05.012>,
 590 2020.

591 Danckaert, T., Fayt, C., Van Roozendael, M., De Smedt, I., Letocart, V., Merlaud, A., and Pinardi, G.: QDOAS Software user
 592 manual, Belgian Institute for Space Aeronomy, 2016.

593 de Foy, B., Lu, Z., and Streets, D. G.: Satellite NO₂ retrievals suggest China has exceeded its NO_x reduction goals from the
 594 twelfth Five-Year Plan, *Sci Rep*, 6, 35912, <https://doi.org/10.1038/srep35912>, 2016.

595 General, S., Pöhler, D., Sihler, H., Bobrowski, N., Frieß, U., Zielcke, J., Horbanski, M., Shepson, P. B., Stirm, B. H., Simpson,
 596 W. R., Weber, K., Fischer, C., and Platt, U.: The Heidelberg Airborne Imaging DOAS Instrument (HAIDI) – a novel imaging
 597 DOAS device for 2-D and 3-D imaging of trace gases and aerosols, *Atmos. Meas. Tech.*, 7, 3459–3485,
 598 <https://doi.org/10.5194/amt-7-3459-2014>, 2014.

599 Guenther, A., Karl, T., Harley, P., Wiedinmyer, C., Palmer, P. I., and Geron, C.: Estimates of global terrestrial isoprene
 600 emissions using MEGAN (Model of Emissions of Gases and Aerosols from Nature), *Atmos. Chem. Phys.*, 6, 3181–3210,
 601 <https://doi.org/10.5194/acp-6-3181-2006>, 2006.

602 Guenther, A. B., Jiang, X., Heald, C. L., Sakulyanontvittaya, T., Duhl, T., Emmons, L. K., and Wang, X.: The Model of
603 Emissions of Gases and Aerosols from Nature version 2.1 (MEGAN2.1): an extended and updated framework for modeling
604 biogenic emissions, *Geosci. Model Dev.*, 5, 1471–1492, <https://doi.org/10.5194/gmd-5-1471-2012>, 2012.

605 Herman, J., Cede, A., Spinei, E., Mount, G., Tzortziou, M., and Abuhassan, N.: NO₂ column amounts from ground-based
606 Pandora and MFDOAS spectrometers using the direct-sun DOAS technique: Intercomparisons and application to OMI
607 validation, *J. Geophys. Res.*, 114, D13307, <https://doi.org/10.1029/2009JD011848>, 2009.

608 Herman, J., Spinei, E., Fried, A., Kim, J., Kim, J., Kim, W., Cede, A., Abuhassan, N., and Segal-Rozenhaimer, M.: NO₂ and
609 HCHO measurements in Korea from 2012 to 2016 from Pandora spectrometer instruments compared with OMI retrievals and
610 with aircraft measurements during the KORUS-AQ campaign, *Atmos. Meas. Tech.*, 11, 4583–4603,
611 <https://doi.org/10.5194/amt-11-4583-2018>, 2018.

612 Hong, H., Lee, H., Kim, J., Jeong, U., Ryu, J., and Lee, D.: Investigation of Simultaneous Effects of Aerosol Properties and
613 Aerosol Peak Height on the Air Mass Factors for Space-Borne NO₂ Retrievals, *Remote Sensing*, 9, 208,
614 <https://doi.org/10.3390/rs9030208>, 2017.

615 Jeong, U., and H. Hong: Assessment of tropospheric concentrations of NO₂ from the TROPOMI/Sentinel-5 Precursor for the
616 estimation of long-term exposure to surface NO₂ over South Korea, *Remote Sensing*, 13, 1877,
617 <https://doi.org/10.3390/rs13101877>, 2021a.

618 Jeong, U., and H. Hong: Comparison of total column and surface mixing ratio of carbon monoxide derived from the
619 TROPOMI/Sentinel-5 Precursor with In-Situ measurements from extensive ground-based network over South Korea, *Remote*
620 *Sensing*, 13, 3987, <https://doi.org/10.3390/rs13193987>, 2021b.

621 Judd, L. M., Al-Saadi, J. A., Valin, L. C., Pierce, R. B., Yang, K., Janz, S. J., Kowalewski, M. G., Szykman, J. J., Tiefengraber,
622 M., and Mueller, M.: The Dawn of Geostationary Air Quality Monitoring: Case Studies From Seoul and Los Angeles, *Front.*
623 *Environ. Sci.*, 6, 85, <https://doi.org/10.3389/fenvs.2018.00085>, 2018.

624 Judd, L. M., Al-Saadi, J. A., Janz, S. J., Kowalewski, M. G., Pierce, R. B., Szykman, J. J., Valin, L. C., Swap, R., Cede, A.,
625 Mueller, M., Tiefengraber, M., Abuhassan, N., and Williams, D.: Evaluating the impact of spatial resolution on tropospheric
626 NO₂ column comparisons within urban areas using high-resolution airborne data, *Atmos. Meas. Tech.*, 12, 6091–6111,
627 <https://doi.org/10.5194/amt-12-6091-2019>, 2019.

628 Judd, L. M., Al-Saadi, J. A., Szykman, J. J., Valin, L. C., Janz, S. J., Kowalewski, M. G., Eskes, H. J., Veefkind, J. P., Cede,
629 A., Mueller, M., Gebetsberger, M., Swap, R., Pierce, R. B., Nowlan, C. R., Abad, G. G., Nehrir, A., and Williams, D.:
630 Evaluating Sentinel-5P TROPOMI tropospheric NO₂ column densities with airborne and Pandora spectrometers near New
631 York City and Long Island Sound, *Atmos. Meas. Tech.*, 13, 6113–6140, <https://doi.org/10.5194/amt-13-6113-2020>, 2020.

632 Kendrick, C. M., Koonce, P., and George, L. A.: Diurnal and seasonal variations of NO, NO₂ and PM_{2.5} mass as a function of
633 traffic volumes alongside an urban arterial, *Atmospheric Environment*, 122, 133–141,
634 <https://doi.org/10.1016/j.atmosenv.2015.09.019>, 2015.

635 Kim, D., Lee, H., Hong, H., Choi, W., Lee, Y., and Park, J.: Estimation of Surface NO₂ Volume Mixing Ratio in Four
636 Metropolitan Cities in Korea Using Multiple Regression Models with OMI and AIRS Data, *Remote Sensing*, 9, 627,
637 <https://doi.org/10.3390/rs9060627>, 2017.

638 Kim, J., Jeong, U., Ahn, M.-H., Kim, J. H., Park, R. J., Lee, H., Song, C. H., Choi, Y.-S., Lee, K.-H., Yoo, J.-M., Jeong, M.-
639 J., Park, S. K., Lee, K.-M., Song, C.-K., Kim, S.-W., Kim, Y. J., Kim, S.-W., Kim, M., Go, S., Liu, X., Chance, K., Chan
640 Miller, C., Al-Saadi, J., Veihelmann, B., Bhartia, P. K., Torres, O., Abad, G. G., Haffner, D. P., Ko, D. H., Lee, S. H., Woo,
641 J.-H., Chong, H., Park, S. S., Nicks, D., Choi, W. J., Moon, K.-J., Cho, A., Yoon, J., Kim, S., Hong, H., Lee, K., Lee, H., Lee,
642 S., Choi, M., Veeffkind, P., Levelt, P. F., Edwards, D. P., Kang, M., Eo, M., Bak, J., Baek, K., Kwon, H.-A., Yang, J., Park, J.,
643 Han, K. M., Kim, B.-R., Shin, H.-W., Choi, H., Lee, E., Chong, J., Cha, Y., Koo, J.-H., Irie, H., Hayashida, S., Kasai, Y.,
644 Kanaya, Y., Liu, C., Lin, J., Crawford, J. H., Carmichael, G. R., Newchurch, M. J., Lefer, B. L., Herman, J. R., Swap, R. J.,
645 Lau, A. K. H., Kurosu, T. P., Jaross, G., Ahlers, B., Dobber, M., McElroy, C. T., and Choi, Y.: New Era of Air Quality
646 Monitoring from Space: Geostationary Environment Monitoring Spectrometer (GEMS), 101, E1–E22,
647 <https://doi.org/10.1175/BAMS-D-18-0013.1>, 2020.

648 Kley, D. and McFarland, M.: Chemiluminescence detector for NO and NO₂, *Atmos. Technol.*; (United States), 12, 1980.

649 Kowalewski, M. G. and Janz, S. J.: Remote sensing capabilities of the GEO-CAPE airborne simulator, *SPIE Optical*
650 *Engineering + Applications*, San Diego, California, United States, 92181I, <https://doi.org/10.1117/12.2062058>, 2014.

651 Kowalewski, M.G., Janz, S., Al-Saadi, J.A., Good, W., Ruppert, L., Cole, J.: GeoTASO instrument characterization and
652 level1b radiance product generation, In: *Proceedings of the 1st KORUS-AQ Science Team Meeting*, Jeju, South Korea, 27
653 February–3 March 2017, 13, 2017

654 Lamsal, L. N., Martin, R. V., Parrish, D. D., and Krotkov, N. A.: Scaling Relationship for NO₂ Pollution and Urban Population
655 Size: A Satellite Perspective, *Environ. Sci. Technol.*, 47, 7855–7861, <https://doi.org/10.1021/es400744g>, 2013.

656 Lamsal, L. N., Janz, S. J., Krotkov, N. A., Pickering, K. E., Spurr, R. J. D., Kowalewski, M. G., Loughner, C. P., Crawford, J.
657 H., Swartz, W. H., and Herman, J. R.: High-resolution NO₂ observations from the Airborne Compact Atmospheric Mapper:
658 Retrieval and validation, *J. Geophys. Res. Atmos.*, 122, 1953–1970, <https://doi.org/10.1002/2016JD025483>, 2017.

659 Latza, U., Gerdes, S., and Baur, X.: Effects of nitrogen dioxide on human health: Systematic review of experimental and
660 epidemiological studies conducted between 2002 and 2006, *International Journal of Hygiene and Environmental Health*, 212,
661 271–287, <https://doi.org/10.1016/j.ijheh.2008.06.003>, 2009.

662 Lee, K., Yu, J., Lee, S., Park, M., Hong, H., Park, S. Y., Choi, M., Kim, J., Kim, Y., Woo, J.-H., Kim, S.-W., and Song, C. H.:
663 Development of Korean Air Quality Prediction System version 1 (KAQPS v1) with focuses on practical issues, *Geosci. Model*
664 *Dev.*, 13, 1055–1073, <https://doi.org/10.5194/gmd-13-1055-2020>, 2020.

665 Leitão, J., Richter, A., Vrekoussis, M., Kokhanovsky, A., Zhang, Q. J., Beekmann, M., and Burrows, J. P.: On the improvement
666 of NO₂ satellite retrievals–aerosol impact on the airmass factors, *Atmos. Meas. Tech.*, 3, 475–493, [https://doi.org/10.5194/amt-](https://doi.org/10.5194/amt-3-475-2010)
667 3-475-2010, 2010.

668 Leitch, J. W., Delker, T., Good, W., Ruppert, L., Murcray, F., Chance, K., Liu, X., Nowlan, C., Janz, S. J., Krotkov, N. A.,
 669 Pickering, K. E., Kowalewski, M., and Wang, J.: The GeoTASO airborne spectrometer project, SPIE Optical Engineering +
 670 Applications, San Diego, California, United States, 92181H, <https://doi.org/10.1117/12.2063763>, 2014.

671 Levelt, P. F., van den Oord, G. H. J., Dobber, M. R., Malkki, A., Huib Visser, Johan de Vries, Stammes, P., Lundell, J. O. V.,
 672 and Saari, H.: The ozone monitoring instrument, IEEE Trans. Geosci. Remote Sensing, 44, 1093–1101,
 673 <https://doi.org/10.1109/TGRS.2006.872333>, 2006.

674 Lorente, A., Folkert Boersma, K., Yu, H., Dörner, S., Hilboll, A., Richter, A., Liu, M., Lamsal, L. N., Barkley, M., De Smedt,
 675 I., Van Roozendaal, M., Wang, Y., Wagner, T., Beirle, S., Lin, J.-T., Krotkov, N., Stammes, P., Wang, P., Eskes, H. J., and
 676 Krol, M.: Structural uncertainty in air mass factor calculation for NO₂ and HCHO satellite retrievals, Atmos. Meas. Tech., 10,
 677 759–782, <https://doi.org/10.5194/amt-10-759-2017>, 2017.

678 Ma, J. Z., Beirle, S., Jin, J. L., Shaiganfar, R., Yan, P., and Wagner, T.: Tropospheric NO₂ vertical column densities over
 679 Beijing: results of the first three years of ground-based MAX-DOAS measurements (2008–2011) and satellite validation,
 680 Atmos. Chem. Phys., 13, 1547–1567, <https://doi.org/10.5194/acp-13-1547-2013>, 2013.

681 Malm, W. C. and Hand J. L.: An examination of the physical and optical properties of aerosols collected in the IMPROVE
 682 program, Atmospheric Environment, 41, 3407– 3427, <https://doi.org/10.1016/j.atmosenv.2006.12.012>, 2007.

683 Merlaud, A., Constantin, D., Mingireanu, F., Mocanu, I., Maes, J., Fayt, C., Voiculescu, M., Murariu, G., Georgescu, L., Van
 684 Roozendaal, M.: Small whiskbroom imager for atmospheric composition monitoring (SWING) from an unmanned aerial
 685 vehicle (UAV), in: Proceedings of the 21st ESA Symposium on European Rocket & Balloon Programmes and related Research,
 686 Thun, Switzerland pp.9–13, 2013.

687 Meier, A. C., Schönhardt, A., Bösch, T., Richter, A., Seyler, A., Ruhtz, T., Constantin, D.-E., Shaiganfar, R., Wagner, T.,
 688 Merlaud, A., Van Roozendaal, M., Belegante, L., Nicolae, D., Georgescu, L., and Burrows, J. P.: High-resolution airborne
 689 imaging DOAS measurements of NO₂ above Bucharest during AROMAT, Atmos. Meas. Tech., 10, 1831–1857,
 690 <https://doi.org/10.5194/amt-10-1831-2017>, 2017.

691 Merlaud, A., Tack, F., Constantin, D., Georgescu, L., Maes, J., Fayt, C., Mingireanu, F., Schuettmeyer, D., Meier, A. C.,
 692 Schönardt, A., Ruhtz, T., Bellegante, L., Nicolae, D., Den Hoed, M., Allaart, M., and Van Roozendaal, M.: The Small
 693 Whiskbroom Imager for atmospheric composition monitorinG (SWING) and its operations from an unmanned aerial vehicle
 694 (UAV) during the AROMAT campaign, Atmos. Meas. Tech., 11, 551–567, <https://doi.org/10.5194/amt-11-551-2018>, 2018.

695 Nowlan, C. R., Liu, X., Leitch, J. W., Chance, K., González Abad, G., Liu, C., Zoogman, P., Cole, J., Delker, T., Good, W.,
 696 Murcray, F., Ruppert, L., Soo, D., Follette-Cook, M. B., Janz, S. J., Kowalewski, M. G., Loughner, C. P., Pickering, K. E.,
 697 Herman, J. R., Beaver, M. R., Long, R. W., Szykman, J. J., Judd, L. M., Kelley, P., Luke, W. T., Ren, X., and Al-Saadi, J. A.:
 698 Nitrogen dioxide observations from the Geostationary Trace gas and Aerosol Sensor Optimization (GeoTASO) airborne
 699 instrument: Retrieval algorithm and measurements during DISCOVER-AQ Texas 2013, Atmos. Meas. Tech., 9, 2647–2668,
 700 <https://doi.org/10.5194/amt-9-2647-2016>, 2016.

701 National Institute of Environmental Research (NIER) and National Aeronautics and Space Administration (NASA): KORUS-
 702 AQ Final Science Synthesis Report, available at <https://espo.nasa.gov/sites/default/files/documents/5858211.pdf>, last access:
 703 27 June 2022, 2020.

704 Nowlan, C. R., Liu, X., Leitch, J. W., Chance, K., A., González Abad, Liu, C., Zoogman, P., Cole, J., Delker, T., Good, W.,
 705 Murcray, F., Ruppert, L., Soo, D., Follette-Cook, M. B., Janz, S. J., Kowalewski, M. G., Loughner, C. P., Pickering, K. E.,
 706 Herman, J. R., Beaver, M. R., Long, R. W., Szykman, J. J., Judd, L. M., Kelley, P., Luke, W. T., Ren, W., and Si-Saadi, J. A.:
 707 Nitrogen dioxide observations from the Geostationary Trace gas and Aerosol Sensor Optimization (GeoTASO) airborne
 708 instrument: Retrieval algorithm and measurements during DISCOVER-AQ Texas 2013, *Atmos. Meas. Tech.*, 9, 2647–2668,
 709 <http://doi.org/10.5194/atm-9-2647-2016>, 2016.

710 Nowlan, C. R., Liu, X., Janz, S. J., Kowalewski, M. G., Chance, K., Follette-Cook, M. B., Fried, A., González Abad, G.,
 711 Herman, J. R., Judd, L. M., Kwon, H.-A., Loughner, C. P., Pickering, K. E., Richter, D., Spinei, E., Walega, J., Weibring, P.,
 712 and Weinheimer, A. J.: Nitrogen dioxide and formaldehyde measurements from the GEOstationary Coastal and Air Pollution
 713 Events (GEO-CAPE) Airborne Simulator over Houston, Texas, *Atmos. Meas. Tech.*, 11, 5941–5964,
 714 <https://doi.org/10.5194/amt-11-5941-2018>, 2018.

715 Palmer, P. I., Jacob, D. J., Chance, K., Martin, R. V., Spurr, R. J. D., Kurosu, T. P., Bey, I., Yantosca, R., Fiore, A., and Li,
 716 Q.: Air mass factor formulation for spectroscopic measurements from satellites: Application to formaldehyde retrievals from
 717 the Global Ozone Monitoring Experiment, *J. Geophys. Res.*, 106, 14539–14550, <https://doi.org/10.1029/2000JD900772>, 2001.

718 Pastel, M., Pommereau, J.-P., Goutail, F., Richter, A., Pazmiño, A., Ionov, D., and Portafaix, T.: Construction of merged
 719 satellite total O₃ and NO₂ time series in the tropics for trend studies and evaluation by comparison to NDACC SAOZ
 720 measurements, *Atmos. Meas. Tech.*, 7, 3337–3354, <https://doi.org/10.5194/amt-7-3337-2014>, 2014.

721 Platt, U.: Differential absorption spectroscopy (DOAS), *Chem. Anal. Series*, 127, 27–83, 1994.

722 Platt, U., Stutz, J.: Differential absorption spectroscopy, in: *Differential Optical Absorption Spectroscopy*, Springer, Berlin,
 723 Heidelberg, pp. 135–174, 2008.

724 Popp, C., Brunner, D., Damm, A., Van Roozendaal, M., Fayt, C., and Buchmann, B.: High-resolution NO₂ remote sensing
 725 from the Airborne Prism EXperiment (APEX) imaging spectrometer, *Atmos. Meas. Tech.*, 5, 2211–2225,
 726 <https://doi.org/10.5194/amt-5-2211-2012>, 2012.

727 Prasad, A. K., Singh, R. P., and Kafatos, M.: Influence of coal-based thermal power plants on the spatial–temporal variability
 728 of tropospheric NO₂ column over India, *Environ Monit Assess*, 184, 1891–1907, <https://doi.org/10.1007/s10661-011-2087-6>,
 729 2012.

730 Qin, K., Rao, L., Xu, J., Bai, Y., Zou, J., Hao, N., Li, S., and Yu, C.: Estimating Ground Level NO₂ Concentrations over
 731 Central-Eastern China Using a Satellite-Based Geographically and Temporally Weighted Regression Model, *Remote Sensing*,
 732 9, 950, <https://doi.org/10.3390/rs9090950>, 2017.

733 Richter, A., Burrows, J. P., Nüß, H., Granier, C., and Niemeier, U.: Increase in tropospheric nitrogen dioxide over China
 734 observed from space, *Nature*, 437, 129–132, <https://doi.org/10.1038/nature04092>, 2005.

735 Schönhardt, A., Altube, P., Gerilowski, K., Krautwurst, S., Hartmann, J., Meier, A. C., Richter, A., and Burrows, J. P.: A wide
 736 field-of-view imaging DOAS instrument for two-dimensional trace gas mapping from aircraft, *Atmos. Meas. Tech.*, 8, 5113–
 737 5131, <https://doi.org/10.5194/amt-8-5113-2015>, 2015.

738 Shah, V., Jacob, D. J., Li, K., Silvern, R. F., Zhai, S., Liu, M., Lin, J., and Zhang, Q.: Effect of changing NO_x lifetime on the
 739 seasonality and long-term trends of satellite-observed tropospheric NO₂ columns over China, *Atmos. Chem. Phys.*, 20, 1483–
 740 1495, <https://doi.org/10.5194/acp-20-1483-2020>, 2020.

741 Skamarock, W., Klemp, J., Dudhia, J., Gill, D., Barker, D., Wang, W., Huang, X.-Y., and Duda, M.: A Description of the
 742 Advanced Research WRF Version 3, UCAR/NCAR, <https://doi.org/10.5065/D68S4MVH>, 2008.

743 Spinei, E., Whitehill, A., Fried, A., Tiefengraber, M., Knepp, T. N., Herndon, S., Herman, J. R., Müller, M., Abuhassan, N.,
 744 Cede, A., Richter, D., Walega, J., Crawford, J., Szykman, J., Valin, L., Williams, D. J., Long, R., Swap, R. J., Lee, Y., Nowak,
 745 N., and Poche, B.: The first evaluation of formaldehyde column observations by improved Pandora spectrometers during the
 746 KORUS-AQ field study, *Atmos. Meas. Tech.*, 11, 4943–4961, <https://doi.org/10.5194/amt-11-4943-2018>, 2018.

747 Spurr, R. and Christi, M.: On the generation of atmospheric property Jacobians from the (V)LIDORT linearized radiative
 748 transfer models, *Journal of Quantitative Spectroscopy and Radiative Transfer*, 142, 109–115,
 749 <https://doi.org/10.1016/j.jqsrt.2014.03.011>, 2014.

750 Tack, F., Merlaud, A., Iordache, M.-D., Danckaert, T., Yu, H., Fayt, C., Meuleman, K., Deutsch, F., Fierens, F., and Van
 751 Roozendaal, M.: High-resolution mapping of the NO₂ spatial distribution over Belgian urban areas based on airborne APEX
 752 remote sensing, *Atmos. Meas. Tech.*, 10, 1665–1688, <https://doi.org/10.5194/amt-10-1665-2017>, 2017.

753 Tack, F., Merlaud, A., Meier, A. C., Vlemmix, T., Ruhtz, T., Iordache, M.-D., Ge, X., van der Wal, L., Schuettmeyer, D.,
 754 Ardelean, M., Calcan, A., Constantin, D., Schönhardt, A., Meuleman, K., Richter, A., and Van Roozendaal, M.:
 755 Intercomparison of four airborne imaging DOAS systems for tropospheric NO₂ mapping—the AROMAPEX campaign, *Atmos.*
 756 *Meas. Tech.*, 12, 211–236, <https://doi.org/10.5194/amt-12-211-2019>, 2019.

757 Tack, F., Merlaud, A., Iordache, M.-D., Pinardi, G., Dimitropoulou, E., Eskes, H., Bomans, B., Veefkind, P., and Van
 758 Roozendaal, M.: Assessment of the TROPOMI tropospheric NO₂ product based on airborne APEX observations, *Atmos. Meas.*
 759 *Tech.*, 14, 615–646, <https://doi.org/10.5194/amt-14-615-2021>, 2021.

760 Tzortziou, M., Parker, O., Lamb, B., Herman, J., Lamsal, L., Stauffer, R., and Abuhassan, N.: Atmospheric Trace Gas (NO₂
 761 and O₃) Variability in South Korean Coastal Waters, and Implications for Remote Sensing of Coastal Ocean Color Dynamics,
 762 *Remote Sensing*, 10, 1587, <https://doi.org/10.3390/rs10101587>, 2018.

763 Valks, P., Pinardi, G., Richter, A., Lambert, J.-C., Hao, N., Loyola, D., Van Roozendaal, M., and Emmadi, S.: Operational
 764 total and tropospheric NO₂ column retrieval for GOME-2, *Atmos. Meas. Tech.*, 4, 1491–1514, [https://doi.org/10.5194/amt-4-](https://doi.org/10.5194/amt-4-1491-2011)
 765 1491-2011, 2011.

766 Vandaele, A. C., Hermans, C., Simon, P. C., Carleer, M., Colin, R., Fally, S., Mérienne, M. F., Jenouvrier, A., and Coquart,
 767 B.: Measurements of the NO₂ absorption cross-section from 42 000 cm⁻¹ to 10 000 cm⁻¹ (238–1000 nm) at 220 K and 294 K,

Journal of Quantitative Spectroscopy and Radiative Transfer, 59, 171–184, [https://doi.org/10.1016/S0022-4073\(97\)00168-4](https://doi.org/10.1016/S0022-4073(97)00168-4), 1998.

Veefkind, J. P., Aben, I., McMullan, K., Förster, H., de Vries, J., Otter, G., Claas, J., Eskes, H. J., de Haan, J. F., Kleipool, Q., van Weele, M., Hasekamp, O., Hoogeveen, R., Landgraf, J., Snel, R., Tol, P., Ingmann, P., Voors, R., Kruizinga, B., Vink, R., Visser, H., and Levelt, P. F.: TROPOMI on the ESA Sentinel-5 Precursor: A GMES mission for global observations of the atmospheric composition for climate, air quality and ozone layer applications, *Remote Sensing of Environment*, 120, 70–83, <https://doi.org/10.1016/j.rse.2011.09.027>, 2012.

Vlemmix, T., Ge, X., de Goeij, B. T. G., van der Wal, L. F., Otter, G. C. J., Stammes, P., Wang, P., Merlaud, A., Schüttemeyer, D., Meier, A. C., Veefkind, J. P., and Levelt, P. F.: Retrieval of tropospheric NO₂ columns over Berlin from high-resolution airborne observations with the spectrolite breadboard instrument, *Atmos. Meas. Tech. Discuss.*, <https://doi.org/10.5194/amt-2017-257>, in review, 2017.

Wiedinmyer, C., Quayle, B., Geron, C., Belote, A., McKenzie, D., Zhang, X., O'Neill, S., and Wynne, K. K.: Estimating emissions from fires in North America for air quality modeling, *Atmospheric Environment*, 40, 3419–3432, <https://doi.org/10.1016/j.atmosenv.2006.02.010>, 2006.

Wiedinmyer, C., Akagi, S. K., Yokelson, R. J., Emmons, L. K., Al-Saadi, J. A., Orlando, J. J., and Soja, A. J.: The Fire INventory from NCAR (FINN): a high resolution global model to estimate the emissions from open burning, *Geosci. Model Dev.*, 4, 625–641, <https://doi.org/10.5194/gmd-4-625-2011>, 2011.

Wold, S., Esbensen, K., and Geladi, P.: Principal component analysis, *Chemometrics and Intelligent Laboratory Systems*, 2, 37–52, [https://doi.org/10.1016/0169-7439\(87\)80084-9](https://doi.org/10.1016/0169-7439(87)80084-9), 1987.

Woo, J.-H., Choi, K.-C., Kim, H. K., Baek, B. H., Jang, M., Eum, J.-H., Song, C. H., Ma, Y.-I., Sunwoo, Y., Chang, L.-S., and Yoo, S. H.: Development of an anthropogenic emissions processing system for Asia using SMOKE, *Atmospheric Environment*, 58, 5–13, <https://doi.org/10.1016/j.atmosenv.2011.10.042>, 2012.

Zoogman, P., Liu, X., Suleiman, R. M., Pennington, W. F., Flittner, D. E., Al-Saadi, J. A., Hilton, B. B., Nicks, D. K., Newchurch, M. J., Carr, J. L., Janz, S. J., Andraschko, M. R., Arola, A., Baker, B. D., Canova, B. P., Chan Miller, C., Cohen, R. C., Davis, J. E., Dussault, M. E., Edwards, D. P., Fishman, J., Ghulam, A., González Abad, G., Grutter, M., Herman, J. R., Houck, J., Jacob, D. J., Joiner, J., Kerridge, B. J., Kim, J., Krotkov, N. A., Lamsal, L., Li, C., Lindfors, A., Martin, R. V., McElroy, C. T., McLinden, C., Natraj, V., Neil, D. O., Nowlan, C. R., O'Sullivan, E. J., Palmer, P. I., Pierce, R. B., Pippin, M. R., Saiz-Lopez, A., Spurr, R. J. D., Szykman, J. J., Torres, O., Veefkind, J. P., Veihelmann, B., Wang, H., Wang, J., and Chance, K.: Tropospheric emissions: Monitoring of pollution (TEMPO), *Journal of Quantitative Spectroscopy and Radiative Transfer*, 186, 17–39, <https://doi.org/10.1016/j.jqsrt.2016.05.008>, 2017.